7 Antidot Samples

> The world changed from having the determinism of a clock to having the contingency of a pinball machine.
>
> *(Heinz Rudolf Pagels, The Cosmic Code)*

7.1 Introduction

7.1.1 Overview

Lateral potential modulations of quasi-two-dimensional carrier gases have been a main focus of the research leading to this thesis. In the present chapter I shall finally report magnetotransport measurements taken on InAs–GaSb double heterostructures (DHETS) that have been modified by imposing a two-dimensional periodic superlattice potential with a lattice period a. All samples investigated in this chapter fall in the range $\lambda_F < a < \ell_f$, with electron concentrations n_e between 7·1 and 12·0 $\times$ 10^{15} cm^{-2}, corresponding to a Fermi wave length λ_F of 30 to 22 nm and an estimated mean free path ℓ_f between 1·5 and 2·7 µm at 4·2 K.[1] For this reason, the exposition of the experimental and theoretical background in Sec. 7.2 concentrates on the features of essentially classical origin resulting from the commensurability of the cyclotron radius R_c and the lattice period a, which are expected in this regime. For the quoted electron concentrations and modulation periods

[1] The electron mobility is difficult to measure because of the effect of the minigap (see Sec. 5.5.3), and the given values, which were obtained from the resistivity in a high magnetic field parallel to the plane of the sample, should be regarded as lower limits.

from 100 to 800 nm, the commensurability condition $2R_c \approx a$ is fulfilled at perpendicular magnetic fields B_z between 0·4 and 1·4 T. This field range is accessible to experiments with comparable ease and there is a temperature window in which potential commensurability peaks will not be obscured by quantum oscillations.

I had originally hoped to employ the high resolution of the local anodic oxidation (LAO) technique to create potential modulations with small periods of only a few λ_F. However, it became clear during the experiments on LAO-modified samples, which are summarized in Sec. 7.4, that the shallow surface modification that could be achieved with this method would be insufficient to generate a sufficiently strong modulation to investigate commensurability effects in this regime. Instead of further pursuing this approach, I chose to revisit the creation of antidot patterns by means of a multistep process involving deep anisotropic plasma etching,[2] and Sec. 7.5 relates comprehensive magnetotransport measurements on electron-rich DHETs patterned by this method.

7.1.2 A Note on Background Subtraction

The DHETs discussed in this thesis exhibit a strong positive magnetoresistance in a magnetic field perpendicular to the plane of the carrier sheets. This is typical for bipolar systems, and may in general terms be understood with the help of the Drude model introduced in Sec. 5.6.1. Consequently, modulations in the magnetoresistance due to the imposed potential can become obscured.[3] It is therefore sometimes desirable to subtract a smooth reference curve for clarity.

While the background in the absence of a potential modulation can be determined by measuring the magnetoresistance of a suitably chosen control sample, subtracting it is usually not helpful. Apart from any commensurability peaks that may appear, the imposed pattern typically affects the shape of the magnetoresistance curve around zero field and may

[2] See Secs. 4.2.6, 4.2.2, and 4.2.4.

[3] This is different from the situation in pure electron gases, in which the perpendicular field magnetoresistance in the absence of a potential modulation is weak and changes become immediately apparent.

change the average electron–hole ratio. The difference then still has a strong field dependence that makes the commensurability features difficult to assess.

Instead, we subtract a smooth curve that has been determined by a standard least-squares fit of an appropriate fit function to the area of interest. Since there is no known analytical model taking into account all contributions to the background,[4] we employ a simple second-order polynomial as the fit function. Such a parabola is the simplest fit function that yields a satisfactory result for background subtraction and has the added advantage that it does not have any inflection points that may lead to spurious peaks in the difference. All magnetoresistance traces in this chapter that have had a background subtracted have been prepared in this way; only the positive field part is used for fitting, and even though the magnetoresistance is symmetric, the fitted parabola is hence not necessarily centred around zero.

7.2 Background

7.2.1 Overview

Several approaches to the periodic structuring of two-dimensional carrier gases are possible, and most of them have been pursued to some extent. The carriers can be subjected to a modulated electric or magnetic field, and the modulation can be periodic in one or two dimensions. The electric potential can be varied directly, by modulating the charge density at a nearby surface—*e.g.*, by creating local variations of surface states or by using a patterned gate electrode [1]—or indirectly, as a piezoelectric potential in a strained material [2]. In both cases, the pattern has to be defined lithographically; in systems such as GaAs–$Al_xGa_{1-x}As$ heterostructures, in which carriers can be created by photoabsorption, a periodic modulation of the carrier concentration can also be achieved by holographic means. The magnetic

[4] It is tempting to use a function of the form $y(x) = a(1 + bx^2)/(1 + cx^2)$ derived from the simple model of Eq. (5.25), as this gives a good apparent fit for most experimental curves. However, the Drude model ignores electron–hole interaction and can in any case not account for the effect of a periodic modulation on the low-field magnetoresistance—the good agreement is merely a result of the large number of parameters. Subtracting such a background usually works fairly well, but may introduce additional artificial peaks.

field can be modulated by bringing the carrier sheet close to superconducting or ferromagnetic structures exhibiting the desired periodicity.

The theoretical treatment of the transport properties in the presence of such modulations has been centred around two complementary approaches: perturbation theory, which is valid for weak periodic components $V(\mathbf{r}) \ll E_\mathrm{F}/e$, and numerical simulations of individual carriers, which are also applicable to antidots and the intermediate range. The pertinent features of modulated quasi-two-dimensional electron gases (2DEGs) are now well understood on the basis of such calculations. In the case of strong modulations the carrier dynamics become fully chaotic.

7.2.2 Weak Modulations

Evidence

The effect of weak lateral modulations on the transport in a 2DEG was first studied in 1989 by Weiss *et al.* [3–5]. They used the persistent photoconductivity effect of GaAs–$Al_xGa_{1-x}As$ heterojunctions to realize, by means of holographic illumination, one-dimensional modulations of the electron density of a 2DEG with a sub-micron period a. At liquid helium temperatures, the magnetoresistance was measured with the current flowing either parallel (ρ_{xx}) or perpendicular (ρ_{yy}) to the direction in which the potential varied. Low-field oscillations appeared, which were periodic in $1/B_z$; the position of the minima of $\rho_{xx}(B_z)$ could be described by the commensurability condition

$$2R_\mathrm{c}(B_z) = (\lambda - \varphi)a; \qquad \lambda \in \mathbb{Z}^+, \tag{7.1}$$

where $R_\mathrm{c}(B_z)$ is the cyclotron radius of the two-dimensional electrons at the Fermi level E_F and $\varphi \approx \frac{1}{4}$ is a phase shift. In ρ_{yy}, much weaker oscillations, which were shifted by half a period, could be observed, while no oscillations were detected in the Hall resistivities ρ_{xy} and ρ_{yx}. The magnetotransport features were later confirmed in similar experiments [1] and have since become known as *Weiss oscillations*.

These studies were soon extended to two-dimensional modulations, for which weaker oscillations were seen in both $\rho_{xx}(B_z)$ and $\rho_{yy}(B_z)$; their phase corresponded to that of the $\rho_{yy}(B_z)$ oscillations in the one-dimensional case [6]. Magnetoresistance oscillations in a periodic *magnetic* field were first reported by Ye *et al.* [2] in 1995; compared to experiments imposing electric field modulations, the minima of the $\rho_{xx}(B_z)$ oscillations were shifted by half a period, corresponding to $\varphi \approx -\frac{1}{4}$ in Eq. (7.1).

Quantum Model

Following the original approach by Gerhardts [5], the magnetoresistance features in the presence of a one-dimensional modulation can be understood by assuming a harmonic modulation of the electric potential $V(x) = V_0 \cos Kx$, where $K \stackrel{\text{def}}{=} 2\pi/a$, and modifying Eq. (5.28) accordingly. The one-dimensional Hamiltonian of the modulated system then becomes

$$\hat{H} = \hat{H}_0 + V(x) = -\frac{\hbar^2}{2m^*}\frac{\partial^2}{\partial x^2} + \frac{e^2 B_z^2 (x - x_0)^2}{2m^*} + V(x), \tag{7.2}$$

where $\hat{H}_0$ is the Hamiltonian in the absence of a modulation and $x_0 = -\hbar k_y / eB_z$ the orbit centre coordinate.[5]

Eq. (7.2) can be diagonalized numerically, or $V(x)$ may be treated as a perturbation to $\hat{H}_0$. In this case, the first-order correction to the energy is

$$\langle \psi_N | V(x) | \psi_N \rangle = V_0 \cos(Kx_0) e^{-X/2} L_N(X), \tag{7.3}$$

where ψ_N is the unperturbed wave function in Landau level N, $X \stackrel{\text{def}}{=} K^2\hbar/2eB_z$, and $L_N(X)$ the N^{th} Laguerre polynomial. For fixed X, $L_N(X)$ oscillates as a function of the index N, leading to a broadening of the individual Landau bands that oscillates with the Landau level index; for $L_N(X) = 0$, the energy correction vanishes and there is no broadening. As the λ^{th} zero of $L_N(X)$ is approximately $X_\lambda^{(N)} \approx \left[(\pi/2)(\lambda - \frac{1}{4})\right]^2 \big/ (N + \frac{1}{2})$, the flat-band condition

[5] In Sec. 5.6.2, $\xi = x - x_0$. This substitution is no longer useful, as the eigenvalues are no longer independent of the orbit position if a modulation is present.

in terms of the cyclotron radius $R_c^{(N)} = (2/K)\left[X_\lambda^{(N)}(N+\frac{1}{2})\right]^{1/2}$ of the N^{th} Landau Level is $2R_c^{(N)} = (\lambda - \frac{1}{4})a$. If $R_c^{(N)}$ is identified with the cyclotron radius at E_F, Eq. (7.1) is recovered.

The eigenstates $\psi_N^{(x_0)}$ of $\hat{H}$ have a finite group velocity and carry current in the y-direction [5]:

$$\left\langle \psi_N^{(x_0)} \middle| \hat{v}_y \middle| \psi_N^{(x_0)} \right\rangle = -\frac{1}{\omega_c}\frac{\partial E_N(x_0)}{\partial x_0}, \tag{7.4}$$

where $E_N(x_0)$ is the energy eigenvalue in the N^{th} Landau level. Using Kubo's linear response theory [7] (see Appendix B) with the assumption of a constant relaxation time τ, the contribution to the conductivity σ_{yy} due to such current carrying states can be estimated in terms of the velocity matrix elements as [5]

$$\Delta\sigma_{yy} = -\frac{2e^2}{2\pi}\frac{eB_z}{\hbar}\int_0^a \frac{dx_0}{a}\sum_N \tau f'\left[E_N(x_0)\right]\left|\left\langle \psi_N^{(x_0)} \middle| \hat{v}_y \middle| \psi_N^{(x_0)} \right\rangle\right|^2, \tag{7.5}$$

where $f'(E)$ is the derivative of the Fermi-Dirac distribution. As a consequence of Eqs. (7.5), (7.4), and (7.3), $\sigma_{yy}(B_z)$ exhibits oscillations with minima at magnetic fields for which E_F lies in a flat Landau band. If $\sigma_{xy}^2 \gg \sigma_{xx}\sigma_{xy}$, which is realistic for the 2DEGs originally investigated, $\rho_{xx} \approx \sigma_{yy}/\sigma_{xy}^2$, and the minima in $\rho_{xx}(B_z)$ occur at the same positions, which are given by Eq. (7.1) as explained above.

The remainder of the conductivity is due to scattering between Landau levels; in the unmodulated system, this is the only contribution. The oscillations in ρ_{yy} arise from this term and can be explained by abandoning the assumption of a constant relaxation time [6, 8, 9]. The effect of the impurity potential can then be described with the help of Green's functions in the self-consistent Born approximation. This results in a modulation of the peak height of the density of states oscillations, and the height becomes maximal for those peaks corresponding to flat Landau bands. The components of the conductivity tensor, when calculated using the Kubo formula, are essentially proportional to the square of the density of states, leading to maxima at the flat band condition, Eq. (7.1). The Landau band conductivity discussed in the previous paragraph, which has minima at the same magnetic field values, dominates σ_{yy} (and hence ρ_{xx}) while oscillations with maxima at these positions appear in σ_{xx} (and ρ_{yy})—in agreement with experiment.

On extending the treatment to two-dimensional potentials [6, 8, 9], the bandwidth oscillations for each direction are individually found to be the same as in the one-dimensional case. However, as discussed in the description of the Hofstadter spectrum (see Sec. 1.2), each Landau level is split into subbands; if the electron mobility is high enough that the splitting between a given pair of subband groups is resolved, the matrix element between corresponding states does not contribute to $\Delta\sigma_{yy}$ and the band conductivity is accordingly strongly suppressed for high mobility samples. In this case, the observable oscillations are dominated by the density of states and ρ_{xx}, like ρ_{yy}, has maxima at the fields given by Eq. (7.1).

Vasilopoulos and Peeters [10, 11] as well as Xue *et al.* [12] have used the same *Ansatz* for weak magnetic modulations $B_z^{(\mathrm{m})}(x) = B_0 \cos Kx$. The magnetic vector potential in the Landau gauge is $\mathbf{A} = \big[0, B_z x + (B_0/K)\sin Kx, 0\big]$ and the Hamiltonian becomes $\hat{H} = \hat{H}_0 + \hat{H}_1$, where

$$\hat{H}_1 = \frac{\omega_1}{K}(\hat{p}_y + eB_z x)\sin(Kx) + \frac{m^*\omega_1^2}{4K^2}\big[1 - \cos(2Kx)\big] \tag{7.6}$$

can be treated as a perturbation if $\omega_1 \stackrel{\mathrm{def}}{=} eB_0/m^* \ll \omega_\mathrm{c}$. Ignoring terms quadratic in ω_1, the first-order correction to the energy is then

$$\big\langle \psi_N \big| \hat{H}_1 \big| \psi_N \big\rangle = \hbar\omega_1 \cos(Kx_0) e^{-X/2}\left[L_{N-1}^{(1)}(X) + \frac{1}{2}L_N(X)\right], \tag{7.7}$$

where $L_N^{(1)}$ is a generalized Laguerre polynomial. For large Landau level indices N, the energy correction, and hence the Landau band width, is approximately proportional to $\sin(KR_\mathrm{c} - \pi/4)$, so that flat bands occur for $2R_\mathrm{c} \approx (\lambda + \frac{1}{4})$. Compared to the situation for an electric modulation, the magnetoresistance oscillations are shifted by a quarter period, as observed in experiments.

Semiclassical Model

Since the commensurability oscillations—unlike the Shubnikov–de Haas-oscillations described in Sec. 5.6.3—are not a quantization effect, they can also be described by the classical motion of electrons at the Fermi energy. In such a semiclassical model, one implicitly assumes that transport is ballistic on the scale of the cyclotron orbits, *i.e.*, $\tau \gg 1/\omega_\mathrm{c}$. Beenak-

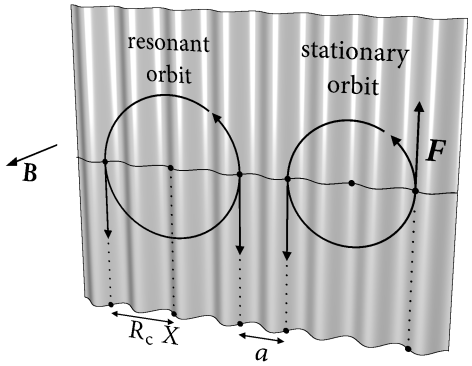

Figure 7.1: One-dimensional guiding centre model

KER [13] has suggested an explanation based on the drift of the *guiding centres* of individual electrons. He defines the guiding centre of a (nearly) free electron at $\mathbf{r}$ having velocity $\mathbf{v}$ as $\mathbf{R} = \mathbf{r} + \hat{\mathbf{z}} \times \mathbf{v}/\omega_c$, where $\hat{\mathbf{z}}$ is the unit vector in the z-direction. In the presence of a potential modulation $V(\mathbf{r})$ giving rise to an electric field $\mathbf{E}(\mathbf{r}) = \nabla_{\mathbf{r}} V(\mathbf{r})/e$, the drift of the guiding centre is $\mathbf{v_R} = \dot{\mathbf{R}} = \hat{\mathbf{z}} \times \mathbf{E}(\mathbf{r})/B_z$. For a weak potential, the cyclotron orbits remain approximately circular and the time average of $\mathbf{v_R}$ can be obtained by integrating the electric field along such orbits:

$$\overline{\mathbf{v}}_{\mathbf{R}}(\mathbf{R}) \approx \frac{1}{2\pi} \int_0^{2\pi} \mathbf{v}_{\mathbf{R}}(\mathbf{R}, \varphi)\, d\varphi = -\frac{1}{2\pi B_z} \int_0^{2\pi} \hat{\mathbf{z}} \times \mathbf{E}\left[\mathbf{R} + \hat{\mathbf{z}} \times \frac{\mathbf{v}(\varphi)}{\omega_c}\right] d\varphi. \tag{7.8}$$

BEENAKKER [13] notes that for a one-dimensional potential with period $a \ll R_c$ the contributions to $\overline{v}_Y(X)$ average out for most of the cyclotron orbit and the integral is dominated by the drift at the extremal points $X \pm R_c$ as shown in Fig. 7.1; here X and Y denote the components of $\mathbf{R}$. He approximates Eq. (7.8) for a harmonic potential of the form $V(\mathbf{r}) = V(x) = V_0 \cos Kx$, and, on averaging over X, finds $\sqrt{\langle \overline{v}_Y^2 \rangle_X} \approx (V_0/m^*\omega_c)\sqrt{K/\pi R_c}\cos(KR_c - \pi/4)$. This drift causes diffusion of the electrons with a diffusion coefficient $\Delta D_{yy} \approx \tau \langle \overline{v}_Y^2 \rangle_X$. One can use the Einstein-Smoluchowski relation $\boldsymbol{\sigma} = e^2 g(E)\mathbf{D}$, where $g(E)$ is the density of states, to calculate the effect of $V(x)$ on σ_{yy}. Since $g(E) = m^*/\pi\hbar^2$ for a 2DEG,

$$\Delta\sigma_{yy} = \frac{e^2 m^* \tau}{\pi\hbar^2} \left\langle \overline{v}_Y^2 \right\rangle_X \approx \frac{e^2\tau}{\pi^2 m^*} \frac{V_0^2}{(\hbar\omega_c)^2} \frac{K}{R_c} \cos^2\left(KR_c - \frac{\pi}{4}\right). \tag{7.9}$$

Eq. (7.9) evidently has minima at the values of $R_c(B_z)$ given by Eq. (7.1), and if $\sigma_{xy}^2 \gg \sigma_{xx}\sigma_{xy}$, these correspond to minima in $\rho_{xx} \approx \sigma_{yy}/\sigma_{xy}^2$. Beenakker is thus able to successfully explain the ρ_{xx} oscillations observed experimentally. While the approximation of the diffusion tensor leads to a small effect on ρ_{yy} and ρ_{xy}, he points out that in a more rigorous calculation of $\mathbf{D}$ based on the Boltzmann equation oscillations are predicted in ρ_{xx} only.

Gerhardts has extended the guiding centre model to arbitrary two-dimensional periodic potentials $V(\mathbf{r}) = \sum_{\mathbf{K}} V_{\mathbf{K}} \exp(i\mathbf{K}\cdot\mathbf{r})$ [14] and commensurate magnetic modulations $B_z^{(\mathrm{m})}(\mathbf{r}) = \sum_{\mathbf{K}} B_{\mathbf{K}} \exp(i\mathbf{K}\cdot\mathbf{r})$ [15,16]. Here $\mathbf{K} \stackrel{\text{def}}{=} 2\pi(n_x/a_x, n_y/a_y)$, a_x and a_y are the periods, and $n_x, n_y \in \mathbb{Z}^+$. $V_{\mathbf{K}}$ and $B_{\mathbf{K}}$ are the Fourier coefficients of the electric and magnetic modulations, respectively. Using $\Delta D_{\mu\nu} \approx \tau\langle \overline{v}_M \overline{v}_N \rangle_{XY}$ (averaging over both X and Y), he arrives at a generalized form of Eq. (7.9):

$$\Delta\sigma_{\mu\nu} \approx \frac{e^2\tau}{\pi m^*(\hbar\omega_c)^2} \sum_{\mathbf{K}} \kappa_{\mu\nu} \left| \operatorname{sgn}(B_z) V_{\mathbf{K}} J_0\big(|\mathbf{K}|R_c\big) + \frac{k_F}{|\mathbf{K}|} \frac{\hbar e B_{\mathbf{K}}}{m^*} J_1\big(|\mathbf{K}|R_c\big) \right|^2, \tag{7.10}$$

where $\kappa_{xx} \stackrel{\text{def}}{=} K_y^2$, $\kappa_{yy} \stackrel{\text{def}}{=} K_x^2$, $\kappa_{xy} \stackrel{\text{def}}{=} -K_x K_y$, k_F is the Fermi wave number, and J_n is the n^{th} order Bessel function of the first kind. While Eq. (7.10) correctly predicts the effect of realistic one-dimensional potential modulations, it cannot fully account for the suppression of the Weiss oscillations seen with two-dimensional potentials.

This suppression can none the less be explained in the semiclassical guiding centre picture [17]: In a two-dimensional superlattice, a large proportion of the *guiding centre* orbits form closed loops, and if the scattering time is sufficiently large, the drift velocity of these orbits averages to zero. One can calculate this effect quantitatively by using a classical Kubo formula[6] (see Appendix B) to derive a more accurate expression for $\boldsymbol{\sigma}$ in terms of the average of the autocorrelation function of the guiding centre velocity. Assuming a constant transport relaxation time τ and negligible broadening of the Fermi contour,

$$\Delta\sigma_{\mu\nu} = \frac{m^* e^2}{\pi\hbar^2} \int_0^\infty e^{-t/\tau} \big\langle v_M(t) v_N(0) \big\rangle^{(E_F)} \, dt, \tag{7.11}$$

[6] Which is equivalent to Chambers' formula under the assumptions made here.

where averaging is now over the phase space at fixed energy E_F [15, 17]. Eq. 7.11 can then be evaluated numerically by simulating a set of guiding centre trajectories corresponding to the required section of the phase space and computing $\left\langle v_N(0)v_M(t)\right\rangle^{(E_F)}$ from it.

7.2.3 Strong Modulations—Antidots

Evidence

Antidot patterns, in which the potential modulation is strong enough to entirely deplete the carrier system in well-defined areas, were first reported by Weiss *et al.* [18] in 1991. They used electron beam lithograph (EBL) and reactive ion etching (RIE) to create a square array of holes with diameter d and sub-micron period a in a GaAs–$Al_xGa_{1-x}As$ heterostructure; the high mobility 2DEG formed at the junction had a mean free path of several micron at liquid helium temperatures. The magnetoresistance ρ_{xx} of such structures showed a number of pronounced peaks in the low field region and a strong increase near $B_z = 0$ compared to an unpatterned sample; in the Hall resistance ρ_{xy}, plateau-like features were seen at the same field values. In contrast to the situation for weak potential modulations, the peaks are not periodic in $1/B_z$ and cannot be described by a simple formula like Eq. (7.1).

Ballistic transport in antidot arrays has since been studied in considerable detail in GaAs–$Al_xGa_{1-x}As$ heterostructures [19, 20]. The effects of large [21] and non-circular [22–24] antidots, as well as generalized rectangular lattices [25] have been investigated. A number of experiments were performed on InAs–GaSb heterostructures [21], which were chosen for the absence of a depletion length at exposed InAs surfaces; in these studies, the GaSb cap layer was very thin and no mobile holes were assumed to be present.

Models

The magnetoresistance peaks in antidot lattices were originally explained by Weiss *et al.* [18] within the semiclassical *pinned orbit* model illustrated in Fig. 7.2. In this model, the cyclotron orbits with radius $R_c(B_z)$ are divided into *scattering* orbits, which collide with antidots,

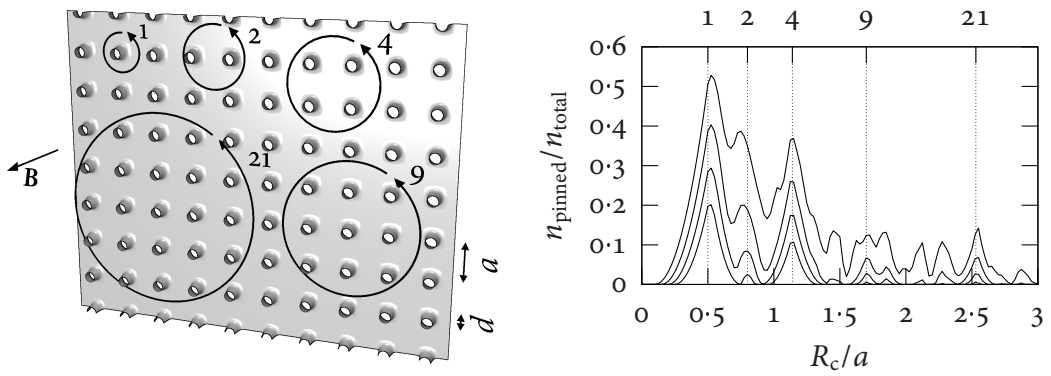

(a) Pinned orbits around 1, 2, 4, 9, and 21 antidots, corresponding to $R_c/a = 0{\cdot}50, 0{\cdot}80, 1{\cdot}14, 1{\cdot}70$, and $2{\cdot}53$.

(b) Proportion of pinned orbits as a function of R_c/a for different values of d/a ranging from 0·5 (bottom) to 0·2 (top) in steps of 0·1. The calculation follows Weiss *et al.* [18].

Figure 7.2: Pinned orbit model.

drifting orbits, which drift without encountering antidots at all, and *pinned* orbits, which encircle a number of antidots without colliding with them. It is assumed that pinned orbits become localized and do not contribute to conduction since the potential gradient close to the antidots guides the electrons and counteracts their drift in the Hall field $E_y^{(H)}$. The proportion of the different types of orbits depends on $R_c(B_z)/a$ and d/a; the fraction of pinned orbits is high if $R_c(B_z)$ has values that allow the cyclotron orbits to fit exactly around a specific number of antidots. For smaller (rescaled) dot diameters d/a, more pinned orbits become possible, yet the peak positions stay approximately constant except for the resonance corresponding to cyclotron orbits encircling two antidots.[7] The magnetoresistance $\rho_{xx}(B_z)$ exhibits peaks at the values of B_z for which the proportion of pinned orbits attains a local maximum. The pinned orbit model predicts peak positions that are in good agreement with a large number of experimental results but makes several *ad hoc* assumptions.

A more robust approach consists in directly calculating electron trajectories by numerical integration of the equations of motion for a suitable model potential (see Appendix C). A chaotic orbit near a commensurability resonance that has been computed in such a way appears in Fig. 7.3. Provided a set of orbits with an appropriate phase space distribution has

[7] The stronger dependence of this peak on d/a is readily understood from geometry, *cf.* Fig. 7.2(a).

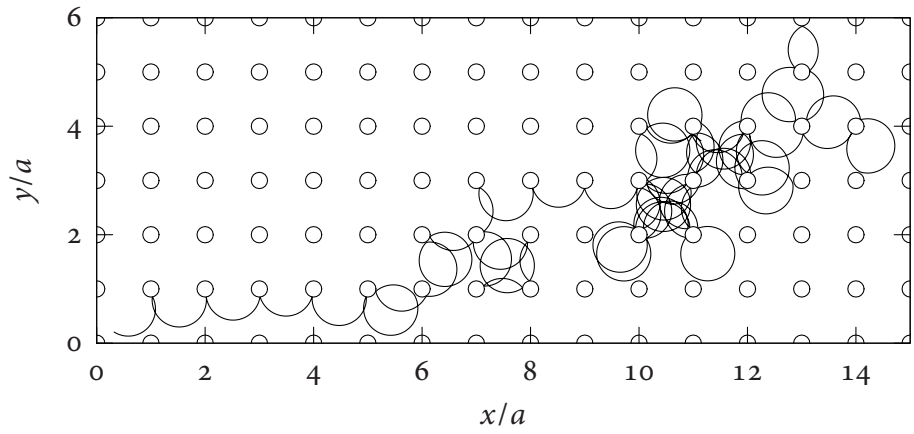

Figure 7.3: Chaotic electron trajectory in an antidot lattice with lattice constant a for $2R_c \approx a$.

been simulated, the conductivity $\boldsymbol{\sigma}$ (and hence the resistivity $\boldsymbol{\rho} = \boldsymbol{\sigma}^{-1}$) can be calculated from the the velocity autocorrelation using a classical Kubo formula [7] in the same way as explained in Sec. 7.2.2 for the motion of guiding centres: assuming a constant phenomenological relaxation time τ, the static conductivity at zero temperature is

$$\sigma_{\mu\nu} = \frac{m^* e^2}{\pi\hbar^2} \int_0^\infty e^{-t/\tau} \left\langle v_\mu(t) v_\nu(0) \right\rangle^{(E_F)} dt, \tag{7.12}$$

where m^* is the effective mass of the electrons and averaging is over the phase space at constant energy E_F (see Appendix B). Such calculations were originally proposed by Fleischmann *et al.* [26] and have since been used extensively by other authors [21, 23, 27–29]. They are easily adapted to different potentials and can be justified whenever the semiclassical approximation is valid, *i.e.*, carriers that participate in scattering can be regarded as moving ballistically with an energy determined by the Fermi level E_F.

Fig. 7.4 shows the resistivity simulated for a steep antidot potential. The positions of the peaks in the diagonal components of $\boldsymbol{\rho}$ (corresponding to the longitudinal resistance) closely mirror those predicted by the pinned orbit model. The off-diagonal components (corresponding to the Hall resistance) exhibit corresponding derivations from linearity. For small dot diameters d/a, step structures similar to those observed in the original experiments [18] appear, which gradually change to dips for large d/a. A careful consideration of phase-space

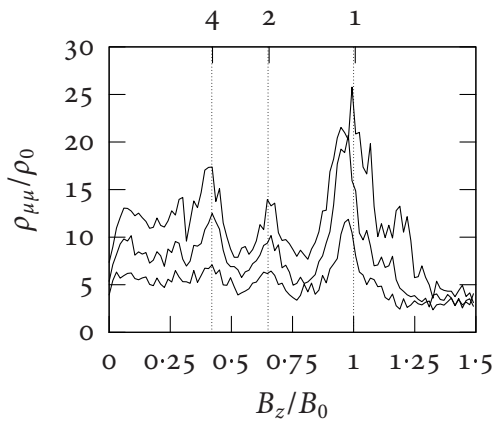

(a) Diagonal components of the resistivity tensor as a function of B_z for $d/a = 0{\cdot}2$ (bottom), 0·3, and 0·4.

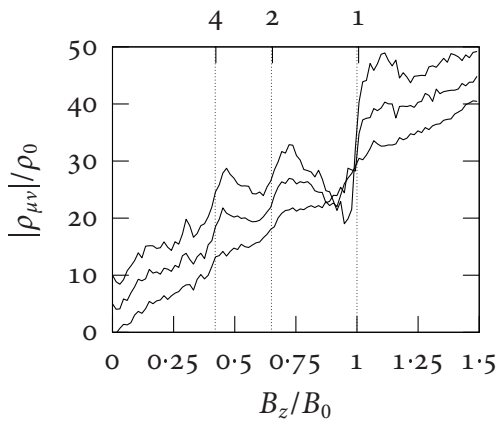

(b) Off-diagonal (Hall) components of the resistivity tensor as a function of B_z for $d/a = 0{\cdot}2$ (bottom), 0·3, and 0·4. The curves are offset by $5\rho_0$ for clarity.

Figure 7.4: Calculating the resistivity via semiclassical simulations. $B_0 = 2m^* v_F/ea$ is the field for which $2R_c = a$ and $\rho_0 = (2\pi\hbar^2)/(m^* e^2 \tau v_F^2)$ is the Drude resistivity.

maps reveals that the contribution to the resistance due to pinned orbits is actually comparatively small. Even if those orbits are disregarded, strong commensurability peaks remain in the calculated resistivity; they can be attributed to chaotic orbits that lie close to the islands of stability that are formed by pinned and precessing orbits and have similar dynamics [26]. Further insight into the physical mechanisms underlying the structure of the classical velocity autocorrelation function may be gained by classifying chaotic skipping orbits according to the direction taken after a small number of hops [27].

7.3 Initial Results

7.3.1 Commensurability Features in the GaSb–InAs–GaSb System

Lateral modulations were first realized in hole-rich InAs–GaSb DHETs by Javed Rehman and Beata Kardynał in Oxford [30]. A number of DHET samples with 300 Å InAs wells and 900 Å GaSb cap layers were patterned with square antidot lattices by electron beam

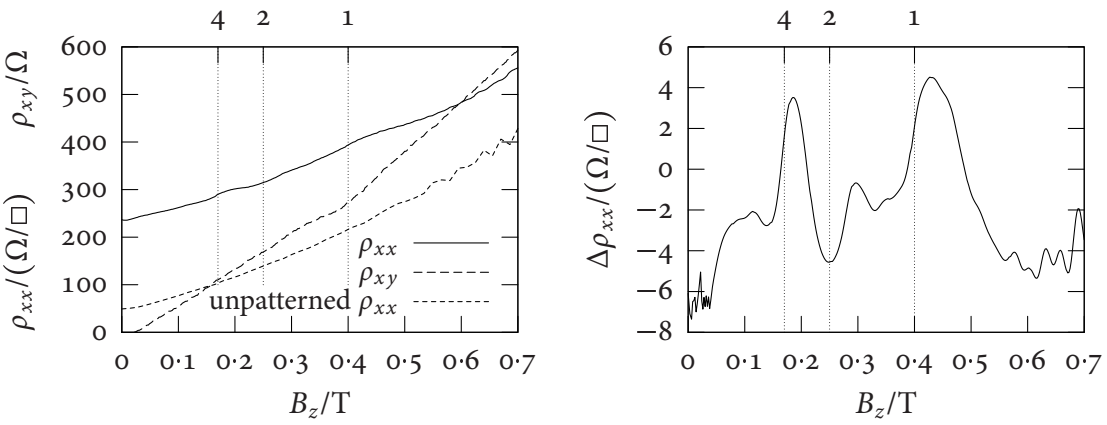

(a) Magnetoresistance and Hall resistance

(b) Magnetoresistance after background subtraction

Figure 7.5: 700 nm antidot lattice on an InAs–GaSb DHET (0X3513) with a 300 Å InAs well and a 900Å GaSb cap [30]. The pattern was created by EBL and transferred by RIE, creating holes with an estimated depth of 140 nm. The dotted vertical lines show the expected commensurability peaks for pinned electron orbits around 1, 2, and 4 antidots calculated using the electron density deduced from the Shubnikov–de Haas-oscillations [18].

lithography. The patterns were transferred by either RIE or wet chemical etching using the tartrate-based etch described in Sec. 4.2.5; it was estimated that the RIE patterns reached down to the InAs layer, while the wet etched patterns took away approximately 60 % of the GaSb cap layer. Modulation periods between 400 and 800 nm were attempted. Given the limited performance of the available electron beam equipment, periods of 650 nm and above could reliably be achieved with this method.

The perpendicular field magnetoresistance of these patterned samples, when measured in a Hall bar geometry at low temperatures (0·3 to 20 K), typically exhibits an increased resistance around zero field and at least two clearly resolved peaks at low magnetic field. At the magnetic field values of the strongest magnetoresistance peaks, the Hall resistance also deviates from its behaviour in unpatterned samples. This behaviour is illustrated in Fig. 7.5 for a typical sample; the features show little reduction in amplitude for temperatures up to 20 K. The position of these peaks could be explained by assuming that they result from the commensurability of electron-like orbits with the imposed modulation according to the pinned

orbit model. The cyclotron radius R_c is calculated from the electron concentration n_e by the free electron expression

$$R_c = \ell_m^2 k_F = \frac{\hbar\sqrt{2\pi n_e}}{eB_z}. \tag{7.13}$$

As explained in Sec 5.5.4, such orbits become possible via magnetic breakdown even though the Fermi contours in the absence of a magnetic field have a more complicated shape owing to electron–hole mixing.

7.3.2 Behaviour in the Parallel Field

Beata Kardynał and I [31] further investigated the behaviour of these samples in the presence of an in-plane magnetic field. According to the reasoning of Sec. 5.5.3, such a magnetic field was expected to decouple the strong interaction of the electrons in the InAs layer with the mobile holes in the GaSb layers close to the interface while having only a small effect on the envelope wave functions in the direction perpendicular to the carrier sheets.

As shown in Fig. 7.6, the behaviour differed significantly between deep dry etched and shallow wet etched samples, which both exhibited similar commensurability features in the absence of an in-plane field. While the commensurability peaks disappeared completely in the wet etched samples for $B_\parallel \geq 4{\cdot}5\,\mathrm{T}$, they persisted in the dry etched samples even if a strong in-plane field was present. Both classes of samples showed small shifts in the peak positions as a function of $B_\parallel$. We tried to explain this behaviour by assuming that the wet-etched pits, being shallower, only represented an antidot potential for the mobile holes in the GaSb; the electrons in the InAs, being of opposite charge, would experience the antidot sites as attractive. While the commensurability features could be assigned to magnetic breakdown orbits closely following the electron cyclotron orbits, the interaction the electrons and holes in the absence of an in-plane field would cause increased scattering of the electrons at the antidots. In a large in-plane field, removal of the interaction would prevent such a scattering mechanism and consequently the appearance of commensurability peaks.

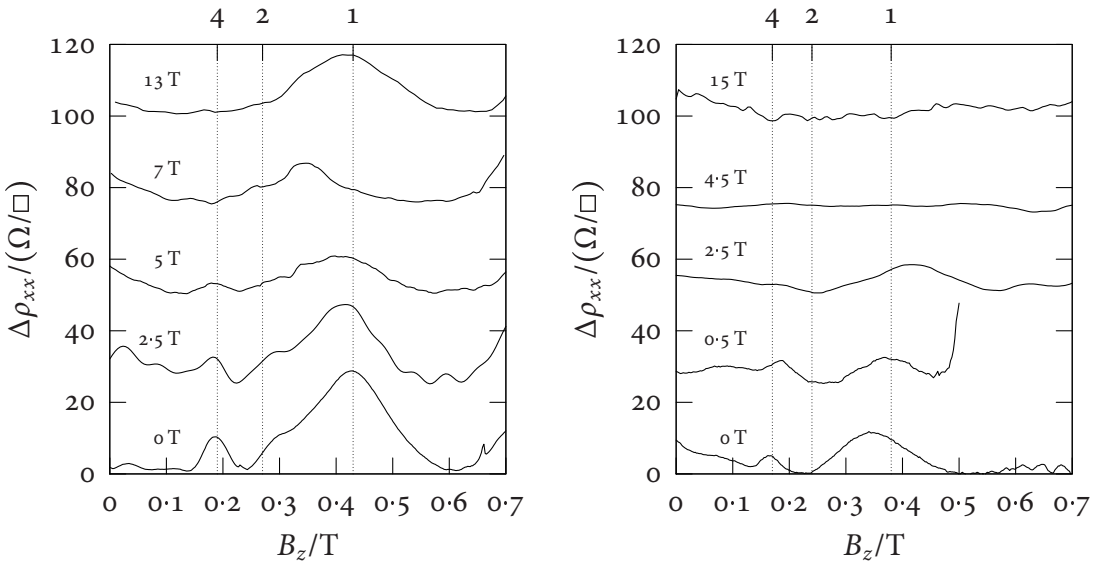

(a) RIE sample (b) Wet etched sample

Figure 7.6: Dry and wet etched antidot samples in a parallel field [31]. The magnetoresistance after background subtraction is shown for several values of the in-plane field $B_\parallel$; the individual curves are shifted by 25 Ω/□. Both samples were produced from InAs–GaSb DHETs with a 300 Å InAs well and a 900 Å GaSb cap and were patterned with a 650 nm period square antidot lattice using EBL. For sample (a), the pattern was transferred into the DHET (OX3251) using RIE and it extends through the InAs layer; sample (b) was created using isotropic wet chemical etching. The dotted vertical lines show the expected commensurability peaks for pinned electron orbits around 1, 2, and 4 antidots calculated using the electron density deduced from the Shubnikov–de Haas-oscillations [18].

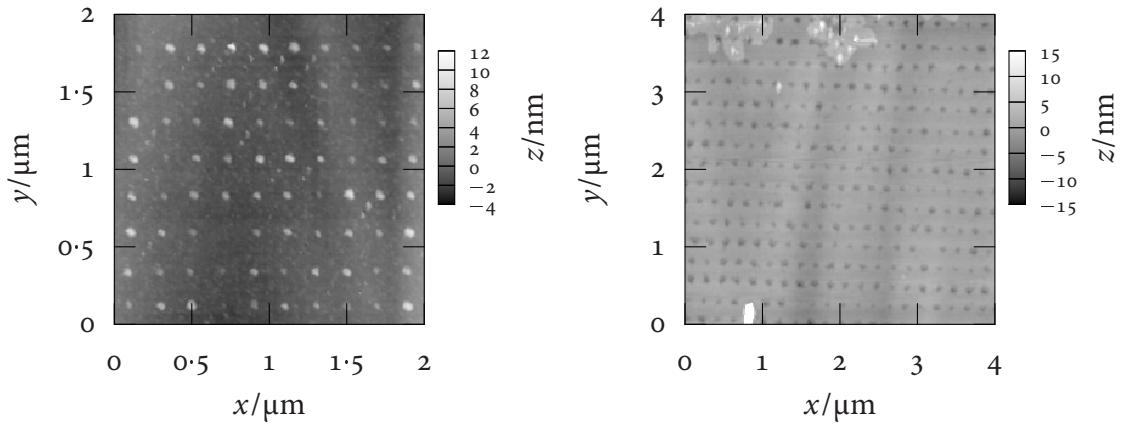

(a) Before removal of oxide

(b) After removal of oxide

Figure 7.7: AFM micrographs of sample OX4531B before and after deoxidation

7.4 Samples Created by Direct Surface Modification

7.4.1 Overview

Using the local anodization technique described in Chapter 3, I prepared a substantial number of samples by patterning the surfaces of Hall bars that were created from substrates containing InAs–GaSb heterostructures. All heterostructures were grown in Oxford using metal-organic vapour phase epitaxy (MOVPE) as explained in Chapter 5. The modifications, which had an aspect ratio of 3 : 1, entirely covered Hall bars with a width of 5 or 10 µm and an aspect ratio of 2 : 1. For the samples discussed in this section, the patterns took the shape of square arrays of dots with a lattice constant a between 100 and 400 nm. The oxide dots had diameters ranging between 50 and 100 nm and were approximately 5 to 10 nm high. This height corresponded to the oxidation of 10 to 20 nm of a GaSb surface layer and was the largest vertical extent of the modification that could be achieved with sufficient reproducibility. I further modified a number of samples by chemically dissolving the oxide (see Chapter 3), leaving pits in place of the dots as seen in Fig. 7.7. Samples of the type discussed here occasionally exhibited a change in behaviour after removal from and reintroduction into a cryogenic experiment. Such degradation was *not* always seen and was not investig-

ated systematically in great detail. Given the sensitivity of the electrical properties to the surface states and the solubility of the GaAs oxide mixture in water, I consider the exposure to condensation, which could not be avoided entirely with some inserts, a likely cause of the problem. Another possible issue that is consistent with measurements is physical damage to the voltage probes.

7.4.2 Double Heterostructures

Patterned double heterostructures comprised both thick (800 to 1,200 Å) cap samples with a high concentration of mobile holes approaching that of the conduction electrons (0x3729, 0x3730, 0x3733, 0x4256, 0x4340) and thin (500 to 700 Å) cap samples that lay in the region of the parameter space for which we previously demonstrated that a change of the cap layer thickness has a large effect on the hole concentration (0x3735, 0x4434, 0x4530, 0x4531, 0x4532).[8] While it was in doubt whether the surface modification with the atomic force microscope (AFM) would create a sufficient potential modulation at the InAs layer to produce a measurable effect in the former set of samples, the previous success with partial removal of the cap layer reported in Sec. 7.3 and the sensitivity of the carrier concentration to the cap thickness led us to expect substantial modulation effects in the latter set—after all, up to 30 % of the cap layer could be affected by the anodization.

None the less, magnetotransport measurements at 0·5 to 4·2 K following the procedure laid down in Chapter 4 revealed no compelling evidence for commensurability features in any of these samples. While various background substitution approaches showed small reproducible resistivity fluctuations above the noise threshold, these were not correlated with the surface modification; the behaviour of the magnetoresistance and Hall resistance was qualitatively similar for both patterned and control Hall bars. The outcome of these experiments is summarized in Table 7.1, which gives a limited number of quantitative results in a concise form. Particular attention is given to the electron concentration, as this quantity is

[8] Chapter 5 explains the influence of the surface states and the cap layer thickness on the electronic properties of the DHET in detail.

Substrate	t_{cap} (Å)	Sample	a (nm)	T (K)	Control Area n_e (10^{11}/cm^2)	Control Area $\rho_{xx}(0)$ (Ω/□)	Patterned Area n_e (10^{11}/cm^2)	Patterned Area $\rho_{xx}(0)$ (Ω/□)
OX4256	1,000	A	400	4·2	7·7	37	7·9	69
		B	400	4·2	7·7	45	8·0	46
		C	400	4·2	7·9	48	8·1	41
OX4434	700	A	200	4·2	8·1	76	7·9	89
OX4340	1,200	A	200	4·2	7·0	186	7·3	173
		B	200	4·2	7·5	186	7·3	210
OX3735	600	A	200	4·2	8·9	214	9·1	221
OX3733	1,200	A	200	4·2	7·6	179	7·6	206
OX3729	800	A	200	4·2	7·6	84	7·5	80
OX3730	1,000	A	200	4·2	7·4	159	7·4	146
		B	200	4·2	7·5	148	7·6	109
		C, deox.	200	4·2	7·0	46	7·0	39
OX4530	700	A	200	4·2	6·8	102	6·8	102
		A	200	10	6·7	113	6·7	113
		A	200	15	6·9	146	6·8	132
		A	200	20	—	197	—	155
		B	400	4·2	7·1	112	7·1	110
		B	400	10	7·3	118	7·2	119
		B	400	15	7·2	143	7·1	142
		B	400	20	—	186	—	183
		C	200	0·5	7·3	88	7·4	94
		D	400	0·5	7·6	81	7·4	89
OX4531	500	A, deox.	100	4·2	7·7	73	7·7	85
		B, deox.	200	4·2	7·9	76	7·9	83
		C, deox.	400	4·2	7·6	79	7·6	73
		C, deox.	400	1·5	7·5	74	7·5	75
OX4532	680	A	200	0·5	7·3	101	7·3	121
		B	400	0·5	7·3	83	7·3	83

Table 7.1: Direct surface modification. The electron concentration n_e was calculated from the frequency of the Shubnikov-de Haas-oscillations in the perpendicular field magnetoresistance; it is accurate to about 2×10^{10} cm^{-2}. The absolute error in the resistivity is determined by the uncertainty in the precise shape and effective aspect ratio of the Hall bar (around 10 %); the error in the resistance measurement is negligible in comparison.

susceptible to the presence of an electrostatic potential and can be extracted from the period of the low-field Shubnikov–de Haas-oscillations directly. In contrast, the resistivity depends on the position of the Fermi energy with respect to the minigap as well as on the carrier concentrations and mobilities.

To investigate the possibility of an *average* effect of the surface modification—such as a net change in the Fermi level pinning or reduced mobilities resulting from increased random scattering—I have collected the number of samples showing a specific qualitative change in the observed quantities in Table 7.2. Changes in the electron concentration, the zero field sheet resistivity, and the amplitude of the Shubnikov–de Haas-oscillations are listed for various groups of experiments. These results confirm the impression given by the data of Table 7.1 in that they do not support any hypothetical trends.

7.4.3 InAs Surface

It is well known that in many circumstances a surface accumulation layer forms at InAs surfaces covered with native oxide. We have created a InAs–GaSb single heterostructure with an exposed InAs top surface (0x4338) by omitting the GaSb cap layer from the MOVPE growth process described in Chapter 5. In such a structure, a sheet of mobile electrons appears that is confined to the InAs layer. Since it is located directly at the surface, this quasi-two-dimensional electron gas (2DEG) may be locally depleted by a shallow surface modification technique such as LAO. Indeed, this has been demonstrated by SASA *et al.* [32, 33] in earlier work on samples of a similar type.

Magnetotransport traces of sample 0x4338 showed spin-split Shubnikov–de Haas-oscillation peaks and no strong positive magnetoresistance or curvature in the Hall resistance, as expected for a 2DEG. The two-dimensional electron density was $13{\cdot}5 \pm 0{\cdot}2 \times 10^{11}\,\mathrm{cm}^{-2}$, while the mobility was $18{,}000 \pm 1{,}000\,\mathrm{cm}^2/(\mathrm{V\,s})$. From this substrate, I prepared and measured at 4·2 K two samples containing square antidot patterns with a lattice period of 200 nm following the approach detailed in Sec. 7.4.2. The magnetoresistance of both the patterned

(a) Carrier concentration

	$n_e^{(pat)} > n_e^{(ctrl)}$	$n_e^{(pat)} \approx n_e^{(ctrl)}$	$n_e^{(pat)} < n_e^{(ctrl)}$
$t_{cap} \leq 700\,Å$	2	9	5
$t_{cap} \geq 800\,Å$	5	3	2
$a \leq 200\,nm$	4	8	4
$a = 400\,nm$	3	4	3
$T = 0{\cdot}5\,K$	1	2	1
$T = 4{\cdot}2\,K$	6	8	3
$T \geq 10\,K$	0	1	3
all samples	7	12	7

(b) Resistivity

	$\rho_{xx}^{(pat)} > \rho_{xx}^{(ctrl)}$	$\rho_{xx}^{(pat)} \approx \rho_{xx}^{(ctrl)}$	$\rho_{xx}^{(pat)} < \rho_{xx}^{(ctrl)}$
$t_{cap} \leq 700\,Å$	8	9	5
$t_{cap} \geq 800\,Å$	3	2	5
$a \leq 200\,nm$	8	3	6
$a = 400\,nm$	2	7	2
$T = 0{\cdot}5\,K$	2	2	0
$T = 4{\cdot}2\,K$	7	4	6
$T \geq 10\,K$	0	3	3
all samples	10	9	9

(c) Amplitude of Shubnikov–de Haas-oscillations

	$A_{SdH}^{(pat)} > A_{SdH}^{(ctrl)}$	$A_{SdH}^{(pat)} \approx A_{SdH}^{(ctrl)}$	$A_{SdH}^{(pat)} < A_{SdH}^{(ctrl)}$
$t_{cap} \leq 700\,Å$	7	6	3
$t_{cap} \geq 800\,Å$	5	0	5
$a \leq 200\,nm$	9	2	5
$a = 400\,nm$	2	5	3
$T = 0{\cdot}5\,K$	1	1	2
$T = 4{\cdot}2\,K$	7	4	6
$T \geq 10\,K$	2	2	0
all samples	12	6	8

Table 7.2: Trends in LAO-modified samples, in numbers of samples satisfying the given conditions. Differences as small as $10^{10}/cm^2$ and $1\,\Omega/\square$ have been taken into account, as small changes in the period of the Shubnikov–de Haas-oscillations can be deduced qualitatively by comparing plots and the effective aspect ratio of two identically manufactured Hall bars on the same sample is consistent. If conservative estimates for the absolute errors are used, there is *no* significant change in any of the experiments.

and the control area exhibited a small (6 ‰) peak at $B_z = 0$ and reproducible fluctuations. However, no correlation between such fluctuations and the presence or absence of the lateral dot superlattice was observed.

7.5 Samples Created by Reactive Ion Etching

7.5.1 Overview

Thanks to the help of Geb Jones, who performed the electron beam exposure in Cambridge, I was also able to create a limited number of deep RIE etched samples which improve on the resolution previously attained for such structures in our group in Oxford. A number of square antidot patterns with a nominal lattice constant between 80 and 400 nm were defined on Hall bars prepared from different substrates and transferred into the semiconductors by means of plasma etching; the exact fabrication method is laid down in Chapter 4. Owing to partial underexposure and peeling of the masks in the RIE, the pattern transfer regrettably did not succeed for the smaller pitch patterns. In the following I shall describe two samples with a period of 400 nm and a physical antidot diameter d/a of $0{\cdot}25 \pm 0{\cdot}05$ determined by AFM measurements, which exhibit notable magnetoresistance features.

Sample OX4531R was created from the DHET OX4531 with a 300 Å InAs well and a 500 Å GaSb cap. The masked sample was placed into a plasma etcher for a sufficient time to remove approximately 140 nm of the semiconductor as estimated from the previously determined etch rates. The pattern transfer was verified with the help of an AFM, establishing a minimum hole etch depth of 30 ± 5 nm and confirming the larger estimated etch depth at the edges of macroscopic mask features. While the observed antidot depth was affected by finite tip size effects, there was considerable evidence from other samples of the same series that the etch depth of holes was less than that of larger features; the difference was attributed to underexposure resulting in incomplete development of the antidots. As a consequence, an

uncertainty remains regarding the actual etch depth, which must lie between the given limits. After processing, the unpatterned control area at 4·2 K had a sheet resistivity of $71 \pm 7\,\Omega/\square$ and an electron concentration determined from the period of the Shubnikov–de Haas-oscillations as $9{\cdot}8 \pm 0{\cdot}2 \times 10^{11}\,\mathrm{cm}^{-2}$. In the presence of a magnetic field $B_\parallel = 18\,\mathrm{T}$ parallel to the surface of the sample, the resistivity dropped to approximately 80 % of its zero field value. Using the high parallel field value, an electron mobility of at least $120{,}000\,\mathrm{cm}^2/(\mathrm{V\,s})$ and a mean free path of at least 2·0 µm were estimated. The electron concentration was significantly increased compared to samples with a similar InAs thickness that were known to have comparable electron and hole concentrations [34]. None the less, the positive perpendicular field magnetoresistance indicated the presence of mobile electron holes; comparing the curvature of the magnetoresistance to the Drude model of Sec. 5.6.1 led to an effective[9] hole concentration of $1{\cdot}6 \times 10^{11}\,\mathrm{cm}^{-2}$.

Sample 0X4532′R was based on the substrate 0X4532 with a 300 Å InAs well and a 680 Å GaSb cap. It was initially etched under the same conditions as 0X4531; there was no significant change in the magnetoresistance as a result of the pattern transfer. The sample was then subjected to another etch step designed to remove an additional 30 nm of the semiconductor; in the absence of an etch mask, one expects the same amount of material to be removed from the flat surface as from the bottom of the antidot pits. Further observation in the AFM confirmed that the antidot pattern was still well resolved. At 4·2 K, the unpatterned control area of the 380 Å cap sample 0X4532′ created by this procedure had a sheet resistivity of $82 \pm 8\,\Omega/\square$ and an electron concentration of $12{\cdot}0 \pm 0{\cdot}2 \times 10^{11}\,\mathrm{cm}^{-2}$. In the presence of a parallel magnetic field $B_\parallel = 18\,\mathrm{T}$, the resistivity dropped to approximately 73 % of its zero field value. The electron mobility and the mean free path estimated from the high parallel field value were at least $85{,}000\,\mathrm{cm}^2/(\mathrm{V\,s})$ and 1·5 µm, respectively. Despite the higher electron density reflecting the reduced cap thickness, the DHET still behaved as a two-carrier system; the effective hole concentration from the Drude model was $1{\cdot}6 \times 10^{11}\,\mathrm{cm}^{-2}$.

[9] As the minigap is not taken into account, this value does not necessarily agree with the actual hole density.

7.5.2 Low Field Commensurability Peaks

Temperature Dependence

The low field magnetoresistivity of sample 0X4531R is shown in Fig. 7.8 for a number of temperatures between 0·5 and 20·0 K. Compared to the control area covered in Fig. 7.8(b), the modulated DHET of Fig. 7.8(a) had a significantly increased zero field resistivity (117 Ω/□ compared to 71 Ω/□). The Shubnikov–de Haas-oscillation amplitude was reduced and the electron concentration increased from $9{\cdot}8 \pm 0{\cdot}2 \times 10^{11}\,\mathrm{cm}^{-2}$ to $13{\cdot}0 \pm 0{\cdot}5 \times 10^{11}\,\mathrm{cm}^{-2}$. The shape of $\rho_{xx}(B_z)$ as a function of the magnetic field differed substantially, being flatter around the origin and exhibiting a single broad peak (α) around $B_z \approx 0{\cdot}8$ T for temperatures up to 10 K. The peak is more readily seen in Fig. 7.8(c), which displays the magnetoresistivity after background subtraction. Its position is consistent with the commensurability between the electron cyclotron orbit of a nearly-free electron gas with the observed electron concentration and the period of the artificial superlattice. In the pinned orbit model, this corresponds to an orbit trapped at a single antidot site; at the magnetic field values corresponding to similar orbits encircling larger groups of antidots, no features were observed in the magnetoresistance.

The corresponding data for 0X4532′R is presented in Fig. 7.9. Comparing patterned and control Hall bars, the electron concentration increased from $12{\cdot}0 \pm 0{\cdot}2 \times 10^{11}\,\mathrm{cm}^{-2}$ to $13{\cdot}4 \pm 0{\cdot}5 \times 10^{11}\,\mathrm{cm}^{-2}$ and the amplitude of the Shubnikov–de Haas-oscillations was reduced. In this sample, the absolute zero field resistivity was similar for the patterned (74 Ω/□ at 4·2 K) and the control region (82 Ω/□ at 4·2 K). Even so, the magnetoresistivity changed as a result of the modulation in a way similar to that seen in 0X4531R, becoming significantly flatter around zero field and exhibiting additional features absent from the control measurements of Fig. 7.9(b). A more complicated peak structure emerged, with a main peak (α) persisting up to 10 K at approximately 0·7 T and an additional higher field peak (β) disappearing at 4·2 K around 2 T. A third peak (γ) might tentatively be assigned to the area between those two features, which exhibited a small resistivity rise at low temperatures. The peaks do not

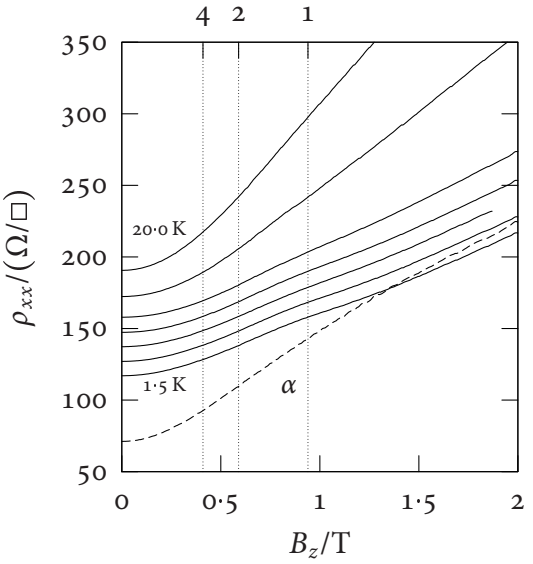

(a) Patterned area. The dashed line corresponds to the unmodified DHET at 1·5 K.

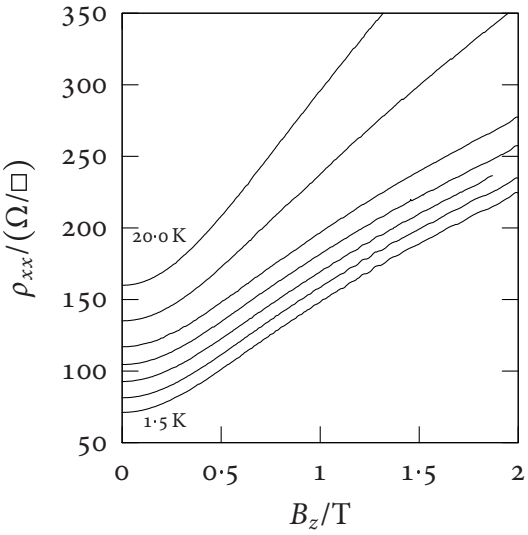

(b) Control area

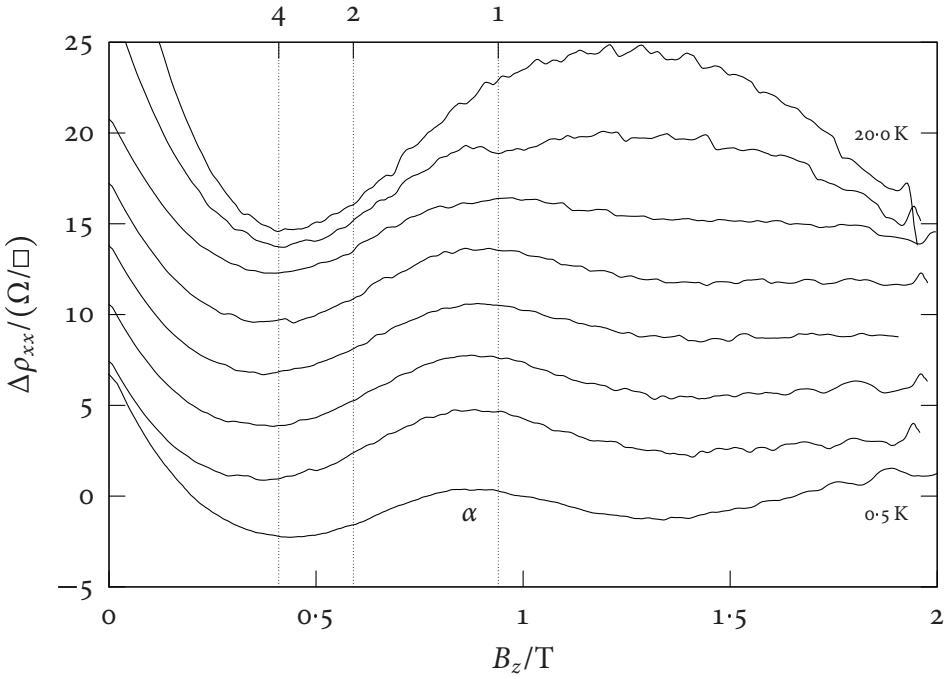

(c) Patterned area after background subtraction

Figure 7.8: Temperature dependence of the low field magnetoresistivity of sample OX4531R. The symmetric part of the measured longitudinal resistivity is shown for (from bottom to top) 0·5, 1·5, 2·5, 4·2, 7·0, 10·0, 15·0, and 20·0 K; the individual curves are offset by 10 Ω/□ in (a) and (b) and 3 Ω/□ in (c) for clarity. Dotted vertical lines show the commensurability condition for pinned electron orbits around 1, 2, and 4 antidots calculated using an electron concentration of $13{\cdot}0 \times 10^{11}\,\mathrm{cm}^{-2}$.

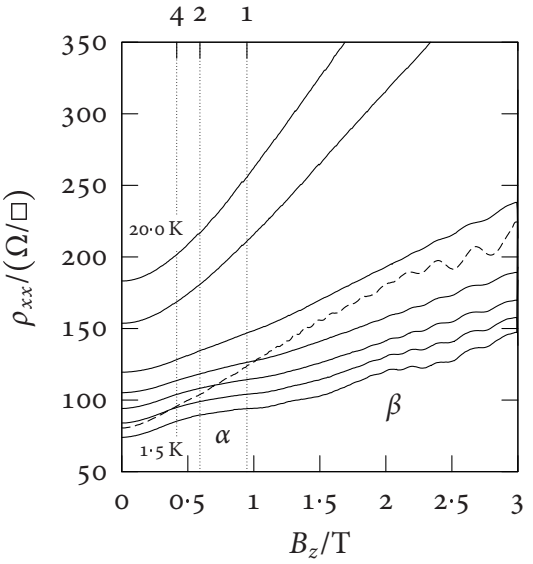

(a) Patterned area. The dashed line corresponds to the unmodified DHET at 1·5 K.

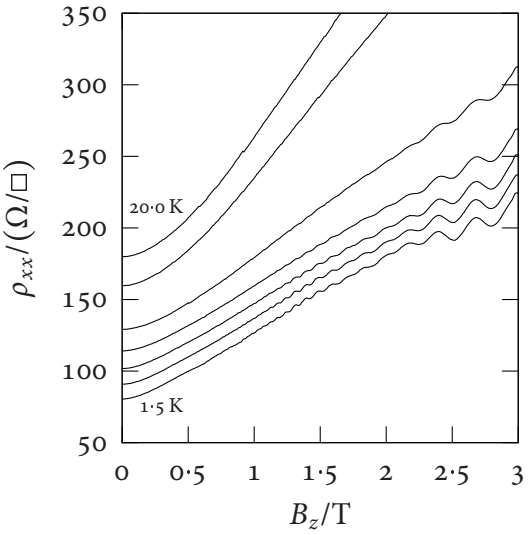

(b) Control area

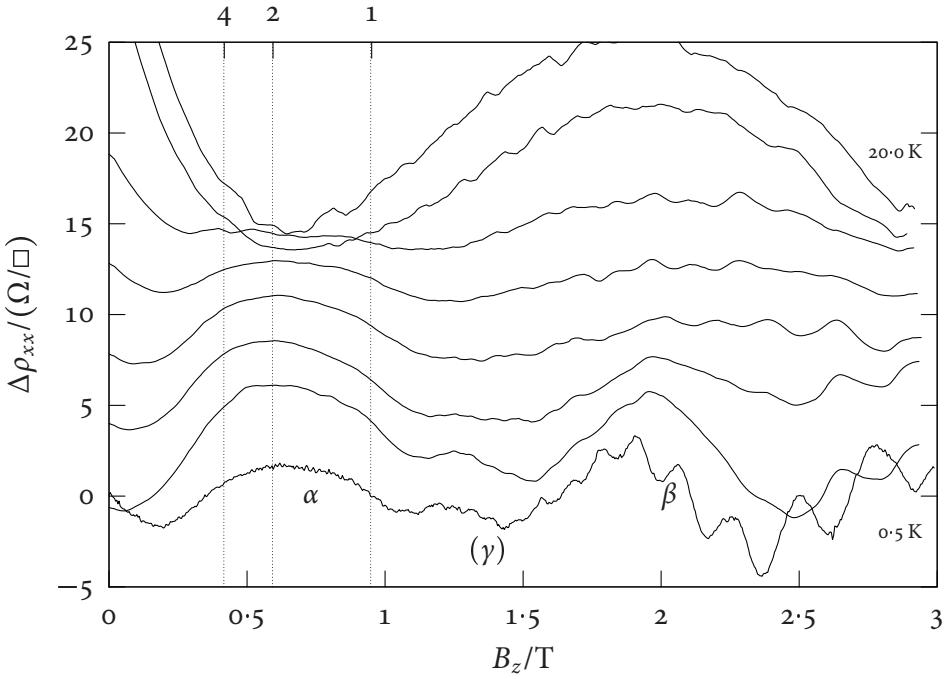

(c) Patterned area after background subtraction

Figure 7.9: Temperature dependence of the low field magnetoresistivity of sample OX4532′R. The symmetric part of the measured longitudinal resistivity is shown for (from bottom to top) 0·5, 1·5, 2·5, 4·2, 7·0, 10·0, 15·0, and 20·0 K; the individual curves are offset by 10 Ω/□ in (a) and (b) and 3 Ω/□ in (c) for clarity. Dotted vertical lines show the commensurability condition for pinned electron orbits around 1, 2, and 4 antidots calculated using an electron concentration of $13{\cdot}2 \times 10^{11}$ cm^{-2}.

Sample	$n_e^{(SdH)}$ ($10^{11}/cm^2$)	R_H (Ω/T)	$n_e^{(R_H)}$ ($10^{11}/cm^2$)
OX4531R	13·0	411	14·2
OX4531 (control)	9·8	630	9·9
OX4532′R	13·4	356	17·1
OX4532′ (control)	12·0	462	13·5

Table 7.3: Hall effect in OX4531R and OX4532′R

directly correspond to commensurability conditions for the electron cyclotron radius R_c, although the primary peak (α) occurs in the magnetic field range where commensurability features are expected. At the position of peak (β), however, $2R_c$ is considerably smaller than the superlattice spacing.

Neither OX4531R nor OX4532′R exhibited any significant features in the Hall resistivity $\rho_{xy}(B_z)$ at the position of the peaks in $\rho_{xx}(B_z)$. The effective Hall coefficient near $B_z = 0$ differed between the modulated and the unmodulated Hall bars. As shown in Table 7.3, the changes were qualitatively consistent with the difference in the electron concentrations determined from the period of the Shubnikov–de Haas-oscillations. Generally, the calculation from the Hall coefficient led to a higher estimate of the electron density; this effect was more prominent for the modulated DHETs and in the case of sample OX4532′.

Parallel Field Dependence

As the presence of a magnetic field in the plane of the DHET affects the formation of the minigap resulting from the mixing of the electron and hole states (*cf.* Sec. 5.5.3) and can influence the commensurability peaks seen in some modulated samples (*cf.* Sec. 7.3.2), I measured the B_z-magnetoresistivity of OX4531 and OX4532′ in various parallel magnetic fields $B_\parallel$ up to 15 T as well as the $B_\parallel$-magnetoresistivity at $B_z \approx 0$. In these experiments, $B_\parallel$ was parallel to the direction of the excitation current and the rotating setup described in Sec. 4.3.1 was used.

The data for sample OX4531R appears in Fig. 7.10. The overall shape of the magnetores-

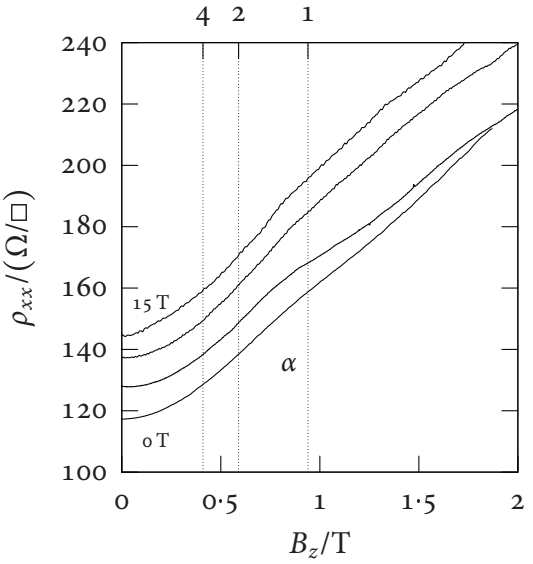

(a) Resistivity as a function of B_z

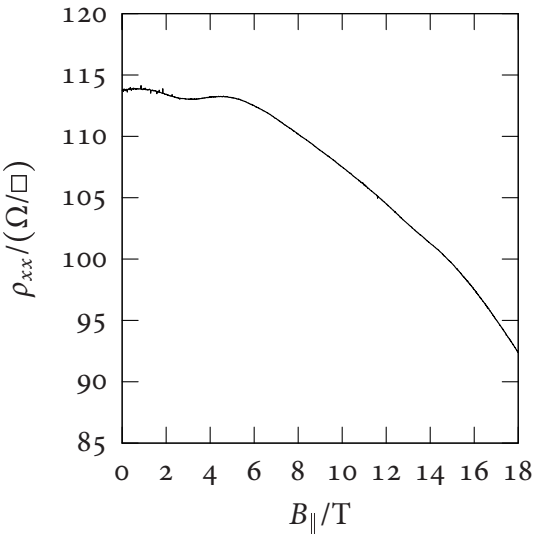

(b) Resistivity at $B_z = 0$ as a function of $B_\parallel$

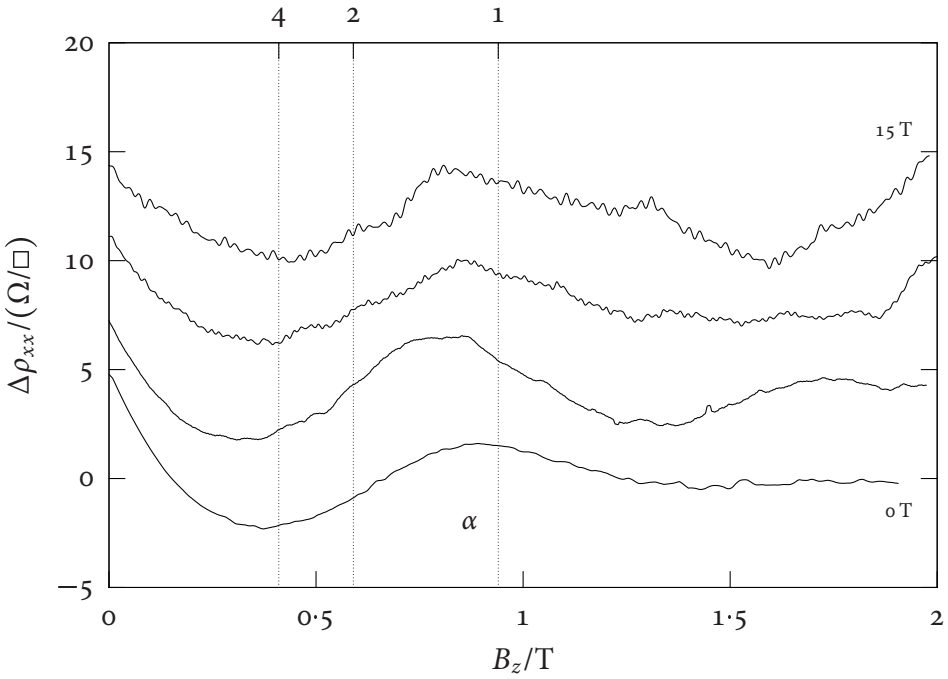

(c) Resistivity as a function of B_z after background subtraction

Figure 7.10: Magnetoresistivity of sample 0x4531R in a parallel field. The longitudinal resistivity measured at 4·2 K while rotating the sample towards $B_\parallel = 0$ is shown for (from bottom to top) $B_\parallel = 0$, 5, 10, and 15 T; the individual plots are shifted by 15 Ω/□ in (a) and 4 Ω□ in (c) for clarity.

istivity, which is seen in Fig. 7.10(a) remains similar. The position and relative magnitude of the commensurability peak (α), best seen after background subtraction in Fig. 7.10(c), did not change significantly in the parallel field. The shape of the peak appeared different, but this may be at least partly attributable to the additional noise appearing in the parallel field measurement as a result of the mechanical movement of the sample. Fig. 7.10(b) shows the resistivity of the modulated Hall bar as a function of the parallel field. There was a significant negative magnetoresistance, with $\rho_{xx}(B_\parallel)$ dropping to 81 % of its zero field value at 18 T; at approximately 5 T it exhibited a local maximum. It is worth noticing that the resistivity did not plateau at the largest observed value of $B_\parallel$ but continued to decrease.

The situation was more complicated in the case of OX4532′R, as can be seen in Fig. 7.11. The well-defined low field peak (α) did not persist in the presence of an in-plane field; at 5 T and 10 T, a small peak at $B_z \approx 1$ T was seen instead, while a broad peak similar to the one seen at $B_\parallel = 0$ T reappeared at 15 T. However, these features were not discernible in all traces. In contrast, the higher field peak (β) maintained a similar size for all values of the parallel field but moved to continuously lower B_z as $B_\parallel$ increased. The small feature (γ) around $B_z \approx 1{\cdot}3$ T persisted with reduced visibility. While its magnitude only barely exceeded the detection threshold given by the noise level on the one hand and the scale of repeatable fluctuations seen in all DHETs on the other hand, it was observable in most low temperature traces. The $B_\parallel$-magnetoresistivity shown in Fig. 7.11(b) resembled that of OX4531R, decreasing continuously with increasing $B_\parallel$. At $B_\parallel = 18$ T, it dropped to approximately 75 % of its zero field value, but did not reach a plateau.

7.5.3 Behaviour in a High Perpendicular Field

Figs. 7.12 and 7.13 show $\rho_{xx}(B_z)$ and $\rho_{xy}(B_z)$ up to $B_z = 18$ T for both the patterned and unpatterned areas of OX4531R and OX4532′R. In both samples, the Shubnikov–de Haas-oscillations in $\rho_{xx}(B_z)$ and the steps in $\rho_{xy}(B_z)$, which mark the onset of Hall plateaux, were less sharply resolved in the modulated regions, while their period in $1/B_z$ was increased.

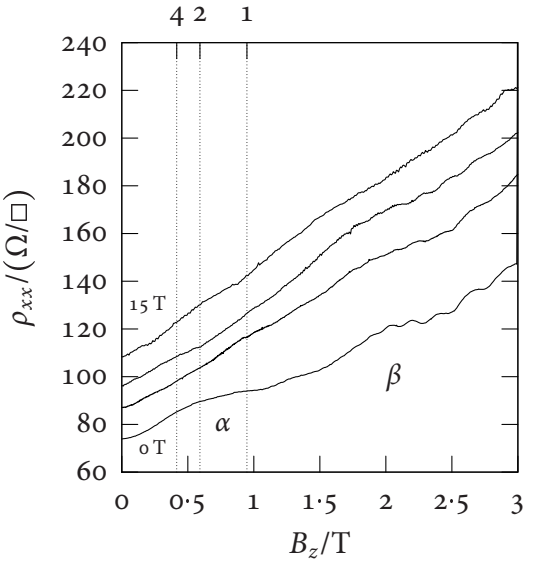

(a) Resistivity as a function of B_z

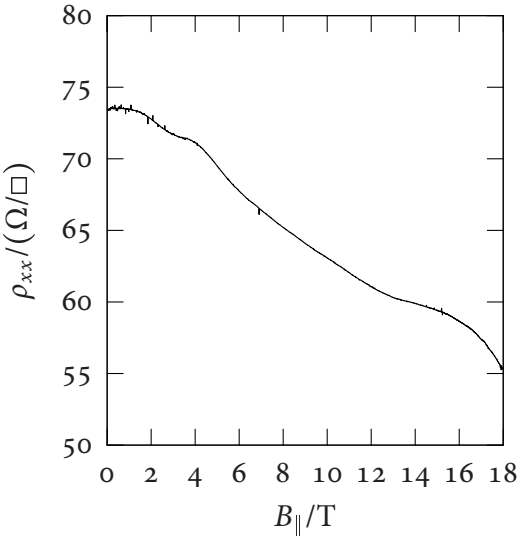

(b) Resistivity at $B_z = 0$ as a function of $B_\parallel$

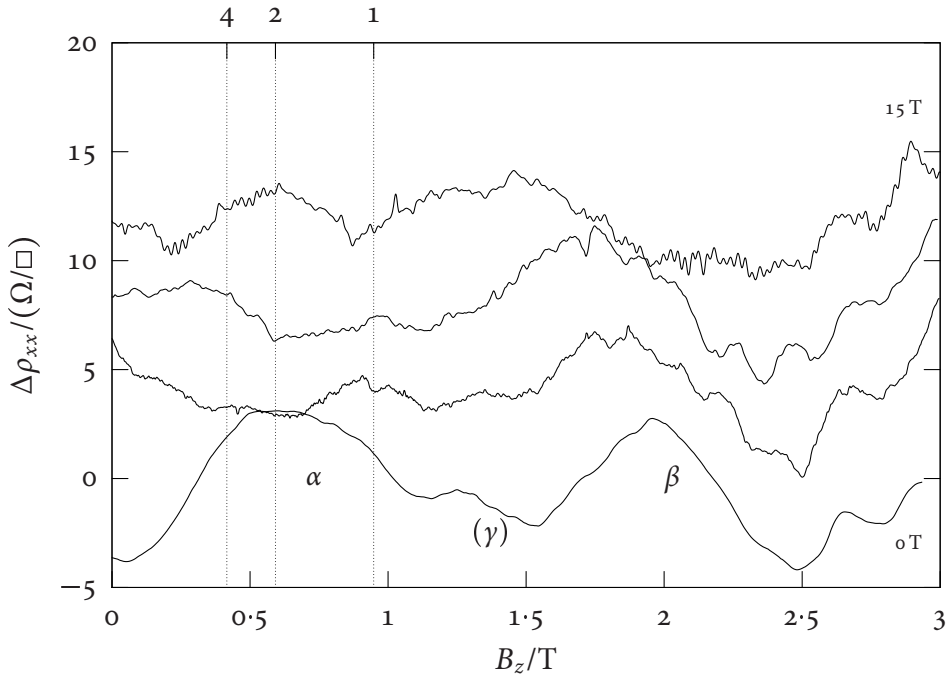

(c) Resistivity as a function of B_z after background subtraction

Figure 7.11: Magnetoresistivity of 0x4532′R in a parallel field. The longitudinal resistivity measured at 4·2 K while rotating the sample towards $B_\parallel = 0$ is shown for (from bottom to top) $B_\parallel = 0$, 5, 10, and 15 T; the individual plots are shifted by 15 Ω/□ in (a) and 4 Ω□ in (c) for clarity.

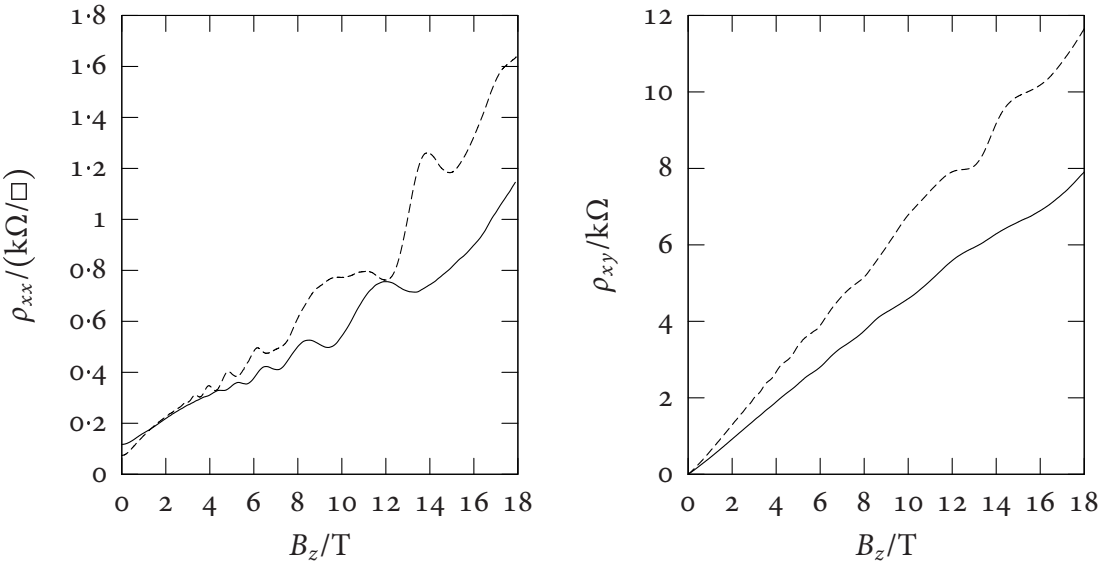

(a) Longitudinal resistivity (b) Hall resistivity

Figure 7.12: High field magnetoresistivity of sample OX4531R. The dashed curves show the data for the unmodified DHET.

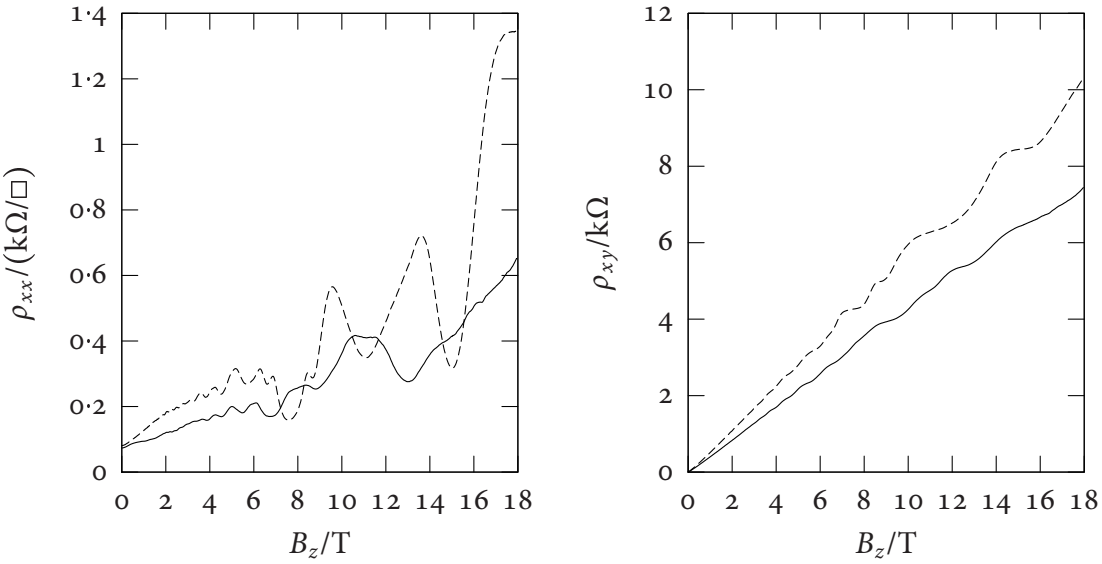

(a) Longitudinal resistivity (b) Hall resistivity

Figure 7.13: High field magnetoresistivity of sample OX4532′R at 0·5 K. The dashed curves show the data for the unpatterned control area.

The Hall resistivity, with the exception of these quantization features, was nearly linear over the entire field range; its slope was reduced as an effect of the antidot lattice. Apart from these observation, the high field measurements taken on the patterned Hall bars did not show qualitatively different behaviour. The Hall resistivity showed a monotonic step-like behaviour without any indication of local minima, as expected from an electron-rich DHET.[10]

7.6 Discussion

7.6.1 General Remarks

In the LAO-patterned samples, if taken collectively, there is no systematic change in the magnetotransport properties that can unambiguously be attributed to the imposed lateral superlattice. Since the DHETs used for these experiments are similar or identical to ones which do show such alterations if modified by a different method, and the inferred mean free paths are considerably longer than the attempted modulation periods, it must be concluded that the effective potential at the carrier sheets in such samples is too weak to bring about a measurable effect. In contrast, the samples prepared by masking and etching show peaks in the magnetoresistance at the approximate field values where the size of the electron cyclotron orbit is commensurate with a dimension of the superlattice. The samples OX4531R and OX4532′R only show a single commensurability peak, and in most experiments the agreement between observed and predicted peak position is not exact.

Several factors contribute to this discrepancy. First of all, since the background that has been subtracted to compensate for the strong positive magnetoresistance is not known *a priori* there is an inherent uncertainty in the measured peak position. The prediction to which the position is compared depends on the chosen analytical model and the measured electron concentration.

[10] See also the discussion in Sec. 6.4.1.

The model itself makes some simplifications, and although the commensurability conditions deduced from the pinned orbit picture agree well with a large range of experimental and simulated magnetoresistance traces, more realistic calculations do not always show an exact agreement. In general, the positions of the peaks relative to the field at which $2R_c = a$ change by a small amount with d/a; calculations based on simulated trajectories suggest a change of approximately 3 % between $d/a = 0{\cdot}2$ and $d/a = 0{\cdot}4$. The position will also depend on the precise shapes of the modulation potential and the electron dispersion.

The electron concentration is determined from the period of the low-field Shubnikov–de Haas-oscillations arising from the same magnetic breakdown orbits as the commensurability features; the calculation is quite reliable as it does not depend on the knowledge of other sample parameters. However, the field range that can be used is limited to the region between the onset of detectable oscillations at 0·4 to 1 T (depending on the electron mobility and the temperature) and the end of the validity of the description in terms of Shubnikov–de Haas-oscillations corresponding to electron orbits at 1 to 4 T (depending on the electron–hole ratio) [34]. In practice, the electron concentrations determined using Eq. (5.32) have an uncertainty between 2 to 8 % depending on the amplitude of the oscillations

More importantly, the calculation of the commensurability condition assumes a spatially uniform electron density, which may not accurately reflect the situation between the antidots in the patterned samples. Following the considerations put forward in Sec. 7.6.3 below, an upper bound on the variation of the electron densitiy in the RIE-etched samples is given by the magnitude of the total increase of 12 to 33 % caused by the patterning.

The parallel field magnetoresistance of OX4531R and OX4532′R, shown in Figs. 7.10(b) and 7.11(b), respectively, differs considerably from thicker cap DHETS such as those discussed in Sec. 7.3, which show a behaviour close to the simulated trace of Fig. 5.8 in Chapter 5. While there is still a significant negative magnetoresistance, indicating the presence of a mixing gap close to the Fermi energy,[11] the resistance drops by a smaller fraction in the region up

[11] For finite temperatures and interaction strengths, there is still an effect even if $E_F - E_0$ exceeds the band offset, so the negative magnetoresistance does not necessarily prove the presence of mobile holes.

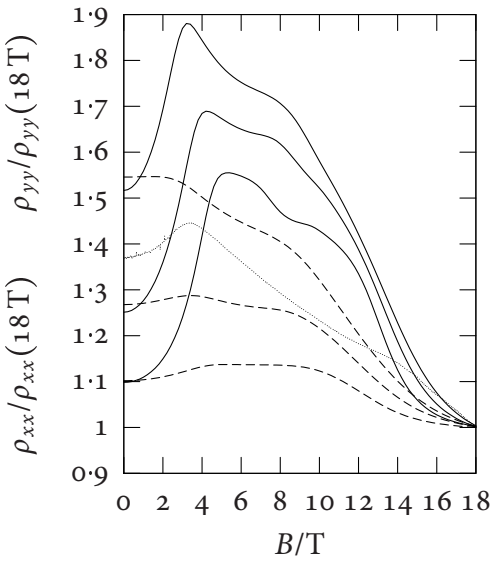

(a) $\Delta = 7\,m\mathrm{eV}$ (bottom), 11 meV, 15 meV (top) for $\delta z = 18\,\mathrm{nm}$

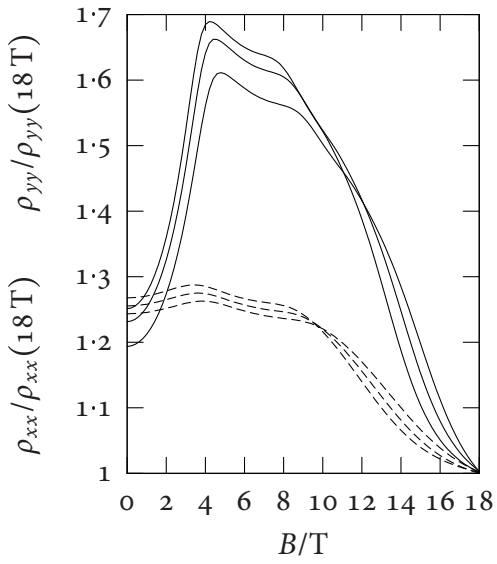

(b) $\delta z = 16\,\mathrm{nm}$ (bottom), 17 nm, 18 nm (top) for $\Delta = 11\,m\mathrm{eV}$

Figure 7.14: Magnetoresistance of thin-cap samples in a parallel magnetic field, calculated at $T = 4{\cdot}2\,\mathrm{K}$ for a DHET with $E_\mathrm{g} = 80\,m\mathrm{eV}$ and $E_\mathrm{F} - E_0 = 78\,m\mathrm{eV}$. The resistivity ρ_{xx} parallel to the in-plane field is shown by solid lines, whereas ρ_{yy} is shown with dashed lines. The single dotted line is the experimental ρ_{xx} of the control area of OX4532′R.

to $B_\parallel = 18\,\mathrm{T}$ and continues to decrease instead of saturating. The electron concentration of $9{\cdot}8 \times 10^{11}\,\mathrm{cm}^{-2}$ in the unpatterned region of sample OX4531R indicates a Fermi level 78 meV above the bottom of the electron band. To match a hole concentration of $1{\cdot}6 \times 10^{11}\,\mathrm{cm}^{-2}$ at the same time, the band offset has to be 80 meV. Using these values, I have calculated several theoretical magnetoresistance traces in Fig. 7.14, varying the electron-hole coupling Δ and the electron-hole separation δz. The larger band offset causes the effect of the minigap to extend over a larger field region compared to Fig. 5.8; for larger interaction strengths and smaller electron–hole separations the field at which the resistivity saturates moves to even higher values. The calculations predict a strong initial increase in the resistivity ρ_{xx} parallel to the in-plane field as the hole Fermi contour approaches the electron Fermi contour from the inside. This increase is small or absent in the experimental curves, which resemble more closely the calculations for ρ_{yy}. The model may not accurately reflect the situation in the

DHET, or the peak may be smeared out by misalignment between current and magnetic field or by local changes in the electron density.

The 2DEG forming in the InAs layer at the surface of the single heterostructure OX4338 has an electron mobility μ_e much lower than that seen in a comparable DHET: as it is located directly at the surface, the electron sheet is very susceptible to scattering from imperfections at the interface. Using the measured values for μ_e and the sheet density n_e, one calculates a mean free path ℓ_f of 350 nm, which is only slightly larger than the modulation period of 200 nm. Under these circumstances, the absence of commensurability features should not come as a surprise. While there is every reason to assume that an antidot potential was created in the 2DEG, the electrons will on average be scattered out of a cyclotron orbit before they can complete it, rendering the pinning mechanism ineffective. It became quickly clear that progress could only be made by procuring higher mobility heterostructures. As similar antidot lattices in pure 2DEGs had been studied in considerable detail and LAO of InAs films had already been demonstrated, I did not consider pursuing this idea a high priority.

7.6.2 Holes

Because of the presence of mobile holes and the peculiar band arrangement, the Fermi contour in InAs–GaSb DHETs has a complex shape resulting from the mixing of the electron and hole dispersion relations and a variety of orbits become possible.[12] So far the discussion has focused on nearly-free electron-like orbits, as they can successfully explain the low-field Shubnikov–de Haas-oscillations and the commensurability peaks; they are recovered in the electron–hole system if the Fermi level intersects the dispersion relation away from the minigap or via magnetic breakdown (*cf.* Sec. 5.5.4) if the cyclotron energy is comparable to the minigap. There is little direct evidence of cyclotron motion corresponding to other sections of the Fermi contour [34].

[12] See Sec. 5.5.3 for a discussion of the details.

Purely hole-like trajectories can be considered directly in the numerical framework developed for electron cyclotron orbits by replacing the parabolic electron dispersion by an anisotropic relation reflecting the hole energy, such as the semi-empirical model introduced in Sec. 5.5.3.[13] As shown in Fig. 7.15, such calculations predict a peak in the hole component of the resistivity at the magnetic field where the orbit size approximately equals the superlattice spacing, similar to the situation in a 2DEG. The higher order peaks are strongly affected by the anisotropy. For the alignment assumed in Fig. 7.15, which to within a few degrees reflects that in the actual samples, the peak corresponding to orbits encircling 2 antidots is completely absent, whereas peaks corresponding to several larger orbits are clearly resolved.

The rough estimate of the hole concentration of $1{\cdot}6 \times 10^{11}\,\mathrm{cm}^{-2}$, obtained from the non-interacting Drude model for both 0X4531R and 0X4532′R, corresponds to $B_0 \approx 0{\cdot}33\,\mathrm{T}$. No feature is seen in the magnetoresistance traces around this field strength. However, the hole mean free path in DHETs of the type investigated here is sufficiently lower than the electron mean free path that the low B_z conductivity is dominated by electronic transport and there is little evidence of Shubnikov–de Haas-oscillations corresponding to cyclotron orbits other than the nearly-free-electron one. It is therefore not surprising that the effects of the commensurability of hole-like orbits with the antidot superlattice on the overall conductivity are not strong enough be measurable.

7.6.3 Surface States, Potential Strength, and Electron-Hole Interaction

In the case of the intermediate sample 0X4532R, it is safe to assume that the antidot etch depth lay between the lower bond of 30 nm established by AFM measurements and an upper bond of 68 nm given by the cap thickness, removing more than 45 % but less than 100 % of the GaSb cap. The sample as originally prepared did not exhibit any characteristic antidot effects, but further etching led to the appearance of such features. The modified sample 0X4532′R has a similar surface structure in the AFM measurement but a significantly increased electron

[13] See also Appendix C for the details of the calculation.

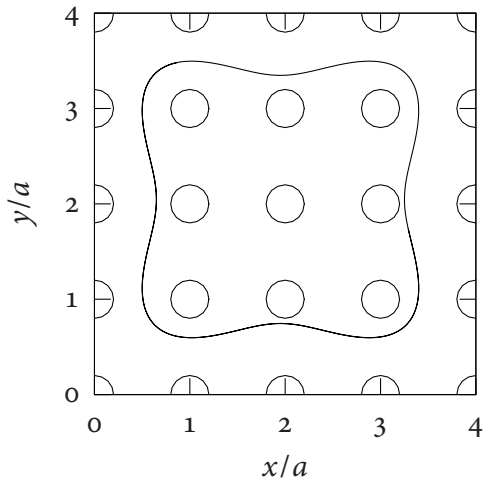

(a) A hole trajectory encircling nine antidots.

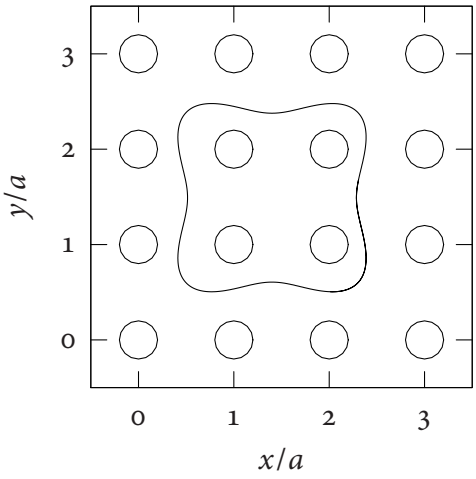

(b) A hole trajectory encircling four antidots.

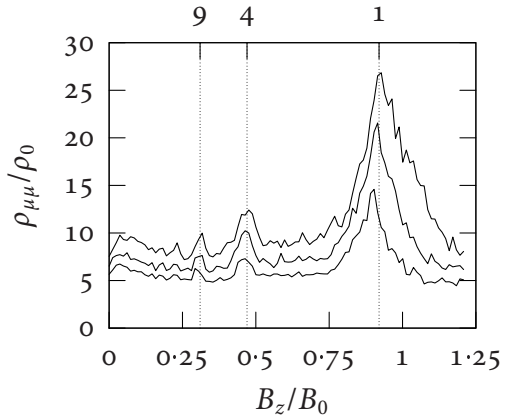

(c) Diagonal components of the resistivity tensor as a function of B_z for $d/a = 0{\cdot}2$ (bottom), $0{\cdot}3$, and $0{\cdot}4$.

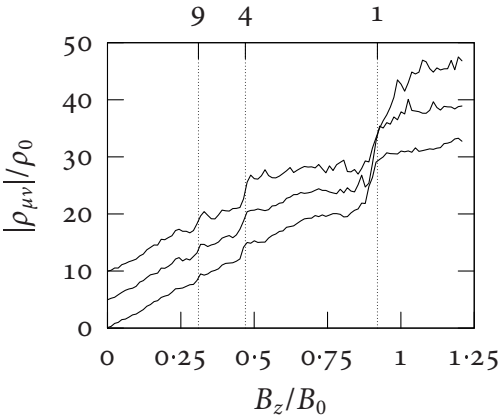

(d) Off-diagonal (Hall) components of the resistivity tensor as a function of B_z for $d/a = 0{\cdot}2$ (bottom), $0{\cdot}3$, and $0{\cdot}4$. The curves are offset by $5\rho_0$ for clarity.

Figure 7.15: Anisotropic hole gas resistivity from semiclassical simulations. It is assumed that the hole gas is parallel to the $\{100\}$ planes, while the superlattice is aligned to the $\langle 100\rangle$ family of crystallographic directions. B_0 is the field for which the cyclotron orbit area is πa^2 and $\rho_0 = (\pi\hbar^2)/(e^2\tau E_\mathrm{F})$.

density deduced from low temperature magnetotransport measurements, in agreement with the expected removal of a similar amount of material from *both* the original surface and the bottom of the etch pits. Based on these observations, the holes now remove at least 80 % of the reduced cap, but may extend through the InAs well. Sample OX4531R was etched under the same conditions; it is therefore plausible, but not inexorable, that a similar upper limit to the hole etch depth applies. In this case, at least 60 % of the cap have been removed, but the antidots may extend into the InAs layer.

These results indicate that locally moving the GaSb surface towards the InAs well by as much as half the original distance in itself is insufficient to elicit a measurable effect on the electronic properties of the embedded DHET. This is true even if the bottom surfaces of the pits lie much closer to the carrier sheets than the lattice constant of the imposed pattern, and wholesale erosion of a comparable amount of the sample surface by the same chemical procedure has a demonstrable influence on the carrier densities. This agrees with the fact that the direct oxidation of the AFM, which, as a surface modification technique, produces similar or shallower features, fails to create a sufficiently strong modulation of the carrier sheets to induce a significant change. On the other hand, it at first seems to be at odds with the behaviour of shallow wet etched samples reported in 7.3.1, despite the fact that these were created from substrates with thicker caps and the potential modulation set up by the surface states was further away from the InAs well.

While the larger dot diameter of the samples created by the nearly isotropic wet chemical etch as well as the larger superlattice constant may play a rôle, the probable explanation of the contradiction is a different one. Whereas the influence of the surface states on the carrier gases is well understood in general and there is considerable evidence supporting the assumption that the Fermi level at oxide passivated GaSb surfaces is pinned above its bulk value [34–36], the precise level of the pinning is expected to be sensitive to the kind of oxide and the presence of contaminations, which in turn can and will vary depending on the fabrication history. This can for example be seen in the data for OX3730 presented in Table 7.1: After removal of the oxide and subsequent reoxidation the electron density is

decreased, although the procedure *reduces* the cap thickness by a small amount.

Both 0X4531R and 0X4532′R show a significant increase of 23 % and 12 %, respectively, in the two-dimensional electron density in the patterned versus the control Hall bars. In contrast, the complete depletion of antidots with $d = a/3$ would lead to a *decrease* of the carrier concentration of 9 %. Since the processing is otherwise identical, the uncertainty associated with the incomplete knowledge of the exact surface states can be largely avoided, so that the antidot pattern must be directly responsible for the effect. The likely mechanism by which it is caused is the Fermi level pinning at the exposed surface of the etch pits. This may be the bottom surface if the pits do not extend into the InAs, but also the side walls. In either case, a significant smooth electric potential modulation is present, either exclusively or in addition to the steep antidot potential, leading to a more complicated effective potential landscape. Fig. 7.16 illustrates schematically the effect of different modulations on the effective potential experienced by both electrons and holes.

As noted in Sec. 7.3.2, the commensurability peaks in shallow wet etched samples disappear in the presence of a magnetic field parallel to the surface. A similar observation can be made for the fundamental peak in 0X4532′R, although the situation at intermediate fields is more difficult to interpret and there is evidence that the peak re-emerges at the highest fields investigated. This behaviour was explained by different potentials for electrons and holes, corresponding to the situation of Fig. 7.16(a). The potential experienced by the electrons would by itself be insufficient to produce strong magnetoresistance peaks, which would be prompted by the local depletion of the interacting hole gas; if the interaction was removed by the parallel field (*cf.* Sec. 5.5.3), the peaks would disappear. Both in these samples and in 0X4532′R, the features disappear in a considerably smaller field than required to fully decouple the electrons and holes; moreover, the exact mechanism by which the electron-hole interaction causes strong commensurability features absent from the non-interacting 2DEG has not been explained satisfactorily. In the light of these problems as well as the small hole concentration and the peak structure in the $B_{\parallel} = 15$ T trace, one cannot necessarily conclude that the parallel field behaviour of 0X4532′R implies a shallow etch depth and a strong contri-

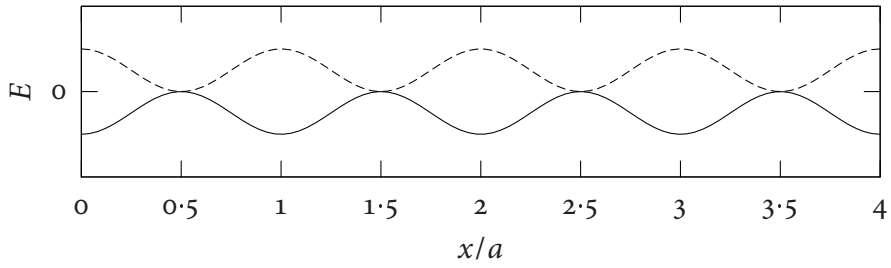

(a) Electrostatic potential

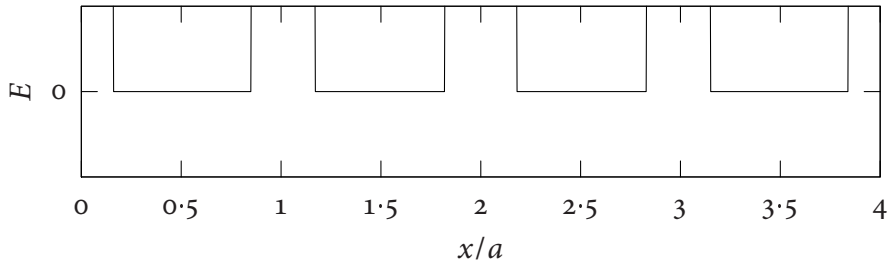

(b) Antidots

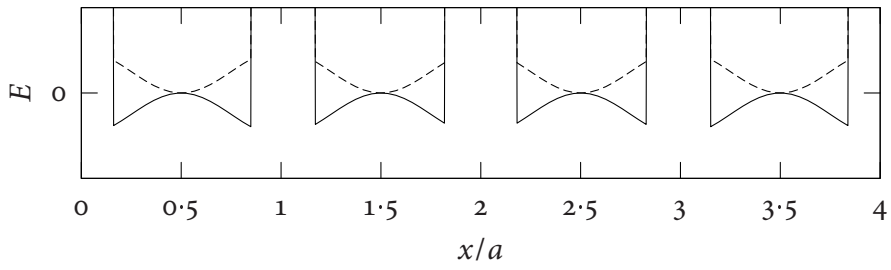

(c) Mixed potential

Figure 7.16: Effective potentials for electrons (solid lines) and holes (dashed lines) along a two-dimensional cross-section through five antidots at $x = 0, a, \ldots, 4a$. The electrostatic potential is assumed to be of sinusoidal form and drop to zero between antidots.

bution of the electron–hole interaction to the observed structure in the magnetoresistivity. A different mechanism by which the parallel magnetic field may affect the size of the commensurability maxima is the size of the gaps in k-space through which carriers must tunnel to complete electron-like magnetic breakdown orbits. The cyclotron energy $\hbar\omega_c$ becomes similar to the minigap $\Delta \approx 7\,\mathrm{m}e\mathrm{V}$ around $B_z = 1\,\mathrm{T}$ and the feasibility of full electron orbits giving rise to the magnetoresistivity features can be expected to be sensitive to the gap size in this field region.

7.6.4 Peak Structure above the Highest Electron Commensurability Field

An interesting and unexpected feature of the magnetoresistance of the sample OX4532′R is the appearance at low temperatures of additional structure above the magnetic field value for which the diameter of the electron cyclotron orbit equals the superlattice spacing. As illustrated in Fig. 7.17, the additional peak is likely a result of the potential modulation; while the control sample shows a small dip on the high field side of the peak position which may also contribute to the measured magnetoresistivity of the patterned Hall bar, the latter exhibits structure that is clearly distinguishable before background subtraction and has no counterpart in the control measurement.

In the pinned orbit model (*cf.* Fig. 7.2), the proportion of pinned orbits decreases in this region until they become impossible where R_c falls below the antidot diameter d. In the region of the putative resistivity peak, all possible orbits are much smaller than a, and an explanation based on commensurability effects is problematic. In contrast, earlier experiments on antidot arrays in 2DEGs have revealed peaks in this field range in the special cases of large diameter [21] or asymmetric [22] antidots. The temperature dependence of these features follows that of the fundamental peak at $2R_c \approx a$.

The observations have been explained by the contribution of different classes of skipping orbits to the conductivity. Eroms *et al.* [21] have published semiclassical simulations following the *Ansatz* of Sec. 7.2.3 that predict a local magnetoresistance maximum around $2{\cdot}5B_0$

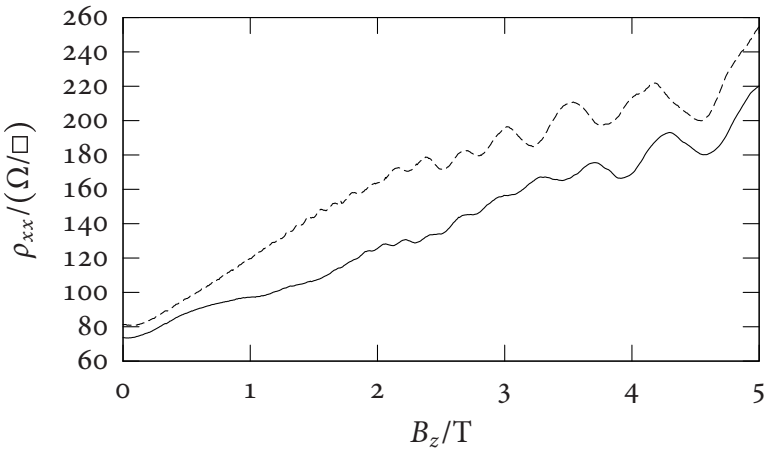

Figure 7.17: Comparison of the 1·5 K magnetoresistivity in sample OX4532′R. The dashed curves show the data for the unpatterned control area.

for large diameter antidots with $d/a \approx 0{\cdot}66$. It has been attributed to quasi-periodic rosette-shaped orbits trapped at single antidots as seen in Fig. 7.18(b). As the simulated resistivities in Fig. 7.18(a) show, I have not been able to reproduce this high field peak, although preliminary calculations have yielded orbits and phase space cross sections similar to those reported. At $B \gg B_0$, most orbits are periodic or quasi-periodic with a slowly decaying autocorrelation function, and the calculated conductivity is sensitive to the accuracy of the simulation, often exhibiting oscillations in B which depend on the time step and cut-off. In all simulations, a further peak develops just above the fundamental peak at $B_z = B_0$, which can be identified with orbits trapped in between antidots; this effect is already indicated in the smaller diameter data of Fig. 7.4(a). There is no corresponding feature in OX4532′R, but the shoulder observed on the commensurability peak in the magnetoresistivity of several larger period antidot lattices on InAs–GaSb DHETs may be attributed to trapped orbits of this kind [30].

In OX4532′R, the high field peak (β) disappears at a relatively low temperature and changes its position in a parallel magnetic field, which is not explained by a semiclassical theory of rosette-shaped orbits. Moreover, the physical etch pit diameter of $0{\cdot}25a$ is much smaller than the antidot size at which the effect is predicted.

Alternatively, a more complicated effective potential similar to that of Fig. 7.16(c) may lie at the origin of the additional higher field structure. Because of the significant effect of the

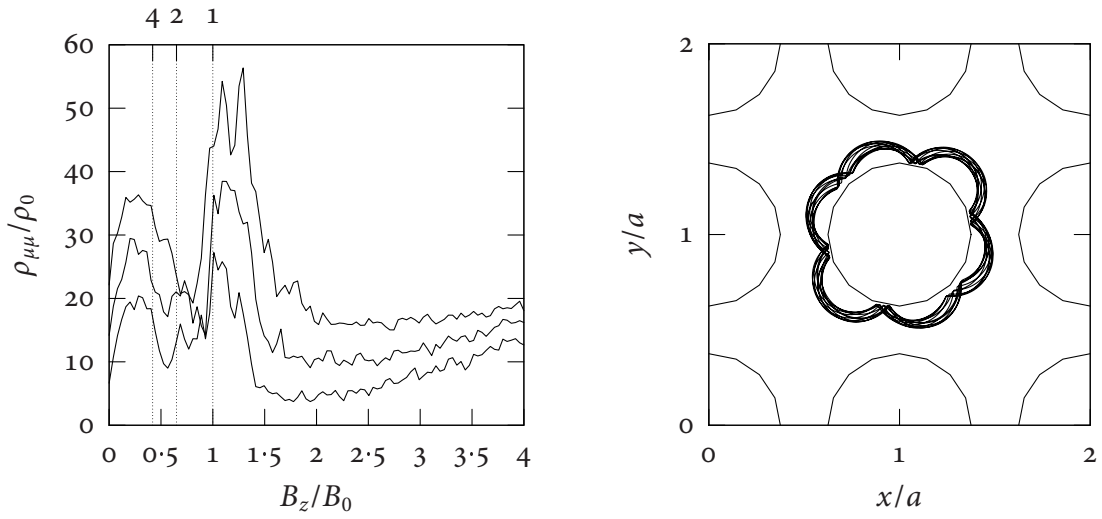

(a) Diagonal components of the resistivity tensor as a function of B_z for $d/a = 0{\cdot}5$ (bottom), 0·6, and 0·7 (top). The curves are offset by $5\rho_0$.

(b) Rosette shaped orbit at $2{\cdot}5B_0$.

Figure 7.18: Calculations for large diameter antidot lattices with $d/a = 0{\cdot}66$. $B_0 = 2m^* v_\mathrm{F}/ea$ is the field for which $2R_\mathrm{c} = a$ and $\rho_0 = (2\pi\hbar^2)/(m^* e^2 \tau v_\mathrm{F}^2)$ is the Drude resistivity.

surface states, it is probable that the potential between antidots is not completely flat, and in this case smaller scale variations are present that could lead to resonances at higher magnetic fields corresponding to smaller cyclotron radii. Halving the distance along the line between two antidots corresponds to a cyclotron radius at twice the magnetic field value B_0 of the fundamental peak, whereas halving the distance along the diagonal of a square formed by four antidots matches a field of $\sqrt{2}B_0$. While the estimate is overly simplistic and one would not necessarily expect commensurability peaks at exactly these magnetic fields, this covers the range of the observed features.

7.7 Conclusions

If modulated by a sufficiently strong two-dimensional superlattice potential with a lattice constant a in the range $\lambda_\mathrm{F} < a < \ell_\mathrm{f}$, high mobility InAs–GaSb DHETs, which contain sheets

of mobile electrons *and* holes, typically show commensurability peaks in the perpendicular field magnetoresistance very similar to those observed in pure 2DEGs. These features persist for temperatures in excess of 20 K for thick cap samples and disappear above 10 K in lower mobility thin cap samples. The peak positions are compatible with electron-like orbits that occur as a result of magnetic breakdown and also manifest themselves in Shubnikov–de Haas quantum oscillations.

Despite the strong interaction between the electrons and holes, the effect of the latter is not apparent. It has been probed by applying an additional magnetic field component parallel to the plane of the carrier sheets, which is known to shift the electron and hole dispersion relations in momentum space. Depending on the sample, the peaks in the magnetoresistance are either unaffected or disappear at a parallel magnetic field lower than that required to completely decouple electrons and holes. For the samples in the latter category, the etch pits cannot be assumed to extend through the InAs layer, so that only the holes see an antidot potential. It has therefore been proposed that the electron-hole coupling is essential for the appearance of commensurability features in these samples; also, the probability of magnetic breakdown may be affected by the changing size of the gaps in momentum space as the in-plane field is varied. A theoretical model that can explain all observations has, however, not been achieved.

A single device, which after an additional etch step has the thinnest GaSb cap of the samples showing commensurability effects, shows further structure of unknown origin above the fundamental peak. The temperature dependence differs, with features disappearing between 2·5 and 4·5 K, and the strongest peak in this region moves to lower perpendicular fields as the parallel field component is increased.

Although LAO can be used to modify GaSb surfaces with high resolution, the method cannot be used to impose an antidot potential on the mobile electrons and holes in typical InAs–GaSb DHETs. In order to maintain an electron mean free path $\ell_f > a$ and avoid full depletion of the hole gas, a minimum GaSb cap depth exceeding the maximum anodization depth is required. While the sensitivity of the carrier gases to the Fermi level pinning at the

free surface implies that a partial removal of the cap layer can be sufficient to create a significant modulation potential, which has been demonstrated in prior experiments on large chemically etched antidots, AFM lithography cannot capitalize on this phenomenon. The probable explanation is that the surface states created by direct anodization or by careful removal of the anodic oxide and reoxidation in air (which preserves the lithographic pattern) are significantly different from those created by the wet etch used earlier and do not set up a sufficiently strong potential at the active layer. This idea is corroborated by the fact that pits etched using RIE and allowed to form a native oxide in air also can remove a significant percentage of the cap thickness without generating an effect on the magnetotransport properties.

Bibliography

[1] R. W. Winkler and J. P. Kotthaus. Landau-band conductivity in a two-dimensional electron system modulated by an artificial one-dimensional superlattice potential. *Physical Review Letters*, 62(10):1177–1180, March 1989.

[2] P. D. Ye, D. Weiss, R. R. Gerhardts, M. Seeger, K. von Klitzing, K. Eberl, and H. Nickel. Electrons in a periodic magnetic field induced by a regular array of micromagnets. *Physical Review Letters*, 74(15):3013–3016, April 1995.

[3] D. Weiss, K. von Klitzing, K. Ploog, and G. Weimann. Magnetoresistance oscillations in a two-dimensional electron gas induced by a submicrometer periodic potential. *Europhysics Letters*, 8(2):179–184, January 1989.

[4] D. Weiss, C. Zhang, R. R. Gerhardts, K. von Klitzing, and G. Weimann. Density of states in a two-dimensional electron gas in the presence of a one-dimensional superlattice potential. *Physical Review B*, 39(17):13020–13023, June 1989.

[5] R. R. Gerhardts, D. Weiss, and K. v. Klitzing. Novel magnetoresistance oscillations in a periodically modulated two-dimensional electron gas. *Physical Review Letters*, 62(10):1173–1176, March 1989.

[6] R. R. Gerhardts, D. Weiss, and U. Wolf. Magnetoresistance oscillations in a grid potential: Indication of a Hofstadter-type energy spectrum. *Physical Review B*, 43(6):5192–5195, February 1991.

[7] R. Kubo. Statistical-mechanical theory of irreversible processes. I. *Journal of the Physical Society of Japan*, 12(6):570–586, 1957.

[8] C. Zhang and R. R. Gerhardts. Theory of magnetotransport in two-dimensional electron systems with unidirectional periodic modulation. *Physical Review B*, 41(18):12850–12861, June 1990.

[9] D. Pfannkuche and R. R. Gerhardts. Theory of magnetotransport in two-dimensional electron systems subjected to weak two-dimensional lattice potentials. *Physical Review B*, 46(19):12606–12626, November 1992.

[10] P. Vasilopoulos and F. M. Peeters. Periodic magnetic modulation of a two-dimensional electron gas: Transport properties. *Superlattices and Microstructures*, 7(4):393–395, 1990.

[11] F. M. Peeters and P. Vasilopoulos. Quantum transport of a two-dimensional electron gas in a spatially modulated magnetic field. *Physical Review B*, 47(3):1466–1473, January 1993.

[12] D. P. Xue and G. Xiao. Magnetotransport properties of two-dimensional electron gases under a periodic magnetic field. *Physical Review B*, 45(11):5986–5990, March 1992.

[13] C. W. J. Beenakker. Guiding-center-drift resonance in a periodically modulated two-dimensional electron-gas. *Physical Review Letters*, 62(17):2020–2793, April 1989.

[14] R. R. Gerhardts. Quasiclassical calculation of magnetoresistance oscillations of a two-dimensional electron gas in an anharmonic lateral superlattice potential. *Physical Review B*, 45(7):3449–3454, February 1992.

[15] R. R. Gerhardts. Quasiclassical calculation of magnetoresistance oscillations of a two-dimensional electron gas in spatially periodic magnetic and electrostatic fields. *Physical Review B*, 53(16):11075, April 1996.

[16] R. Menne and R. R. Gerhardts. Magnetoresistance of a two-dimensional electron gas with spatially periodic lateral modulations: Exact consequences of Boltzmann's equation. *Physical Review B*, 57(3):1707–1722, January 1998.

[17] R. R. Gerhardts and S. D. M. Zwerschke. Guiding-center picture of magnetoresistance oscillations in rectangular superlattices. *Physical Review B*, 64:115322, 2001.

[18] D. Weiss, M. L. Roukes, A. Menschig, P. Grambow, K. von Klitzing, and G. Weimann. Electron pinball and commensurate orbits in a periodic array of scatterers. *Physical Review Letters*, 66(21):2790–2793, May 1991.

[19] M. Wendel, B. Irmer, J. Cortes, R. Kaiser, H. Lorenz, J. P. Kotthaus, A. Lorke, and E. Williams. Nanolithography with an atomic force microscope. *Superlattices and Microstructures*, 20(3):349–356, 1996.

[20] A. Dorn, M. Sigrist, A. Fuhrer, T. Ihn, T. Heinzel, K. Ensslin, W. Wegscheider, and M. Bichler. Electric properties of antidot lattices fabricated by atomic force lithography. *Applied Physics Letters*, 80(2):252–254, January 2002.

[21] J. Eroms, M. Zitzlsperger, and D. Weiss. Skipping orbits and enhanced resistivity in large-diameter InAs/GaSb antidot lattices. *Physical Review B*, 59(12):7829–7832, March 1999.

[22] A. Lorke, S. Wimmer, B. Jager, J. P. Kotthaus, W. Wegscheider, and M. Bichler. Far-infrared and transport properties of antidot arrays with broken symmetry. *Physica B*, 249–251:312–316, 1998.

[23] S. de Haan, A. Lorke, R. Hennig, M. Suhrke, W. Wegscheider, and M. Bichler. Magneto-transport properties of arrays of cross-shaped antidots. *Physical Review B*, 60(12):8845–8848, September 1999.

[24] B. G. L. Jager, S. Wimmer, A. Lorke, J. P. Kotthaus, W. Wegscheider, and M. Bichler. Edge and bulk effects in terahertz photoconductivity of an antidot superlattice. *Physical Review B*, 63, 2001.

[25] J. Rychen, T. Vančura, and T. Heinzel. Commensurability oscillations of rectangular antidot arrays: A classical diffusion model. *Physical Review B*, 58(7):3458–3571, August 1998.

[26] R. Fleischmann, T. Geisel, and R. Ketzmerick. Magnetoresistance due to chaos and nonlinear resonances in lateral surface superlattices. *Physical Review Letters*, 68(9):1367–1370, March 1992.

[27] S. Ishizaka and T. Ando. Detailed analysis of the commensurability peak in antidot arrays with various periods. *Physical Review B*, 55(24):16331–16338, 1997. June.

[28] R. Hennig and M. Suhrke. Absence of commensurability in magnetic antidot arrays with classical chaos. *Physical Review B*, 60(16):11535–11539, October 1999.

[29] R. Onderka, M. Suhrke, and U. Rössler. Anisotropic magnetotransport in a rectangular antidot superlattice: Classical and semiclassical aspects. *Physical Review B*, 62(16):10918–10922, October 2000.

[30] Y. J. Rehman. *Processing and Magneto-transport Studies of InAs/GaSb Low Dimensional Structures*. DPhil thesis, The Queen's College, University of Oxford, 1999.

[31] T. O. Stadelmann, B. Kardynal, R. J. Nicholas, K. Takashina, and N. J. Mason. Magnetotransport studies of antidot superlattices in coupled two-dimensional electron-hole gases. *Physica E*, 12(1–4):293–295, January 2002.

[32] S. Sasa, A. Nakashima, S. Yodogawa, T. Kita, and M. Inoue. Magnetotransport properties of InAs nanostructure devices produced by AFM oxidation. *Physica B*, 314:95–98, 2002.

[33] S. Sasa, A. Nakashima, Y. Nakajima, and M. Inoue. Aharonov–Bohm oscillations observed in nanoscale open-dot structures fabricated in an InAs surface inversion layer. *Physica E*, 20:224–227, 2004.

[34] K. Takashina. *Magneto-transport Studies of GaSb/InAs/GaSb Double-heterostructures*. DPhil thesis, University College, University of Oxford, 2002.

[35] M. Altarelli, J. C. Maan, L. L. Chang, and L. Esaki. Electronic states and quantum Hall effect in GaSb–InAs–GaSb quantum wells. *Physical Review B*, 35(18):9867–9870, June 1987.

[36] C. Petchsingh. *Cyclotron Resonance Studies on InAs/GaSb Heterostructures*. DPhil thesis, Wolfson College, University of Oxford, 2002.